A priori analysis of reduced description of dynamical systems using approximate inertial manifolds

Maryam Akram[a,*], Malik Hassanaly[b], Venkat Raman[b]

[a]*Department of Mechanical Engineering, University of Michigan, Ann Arbor, MI 48109, United States*
[b]*Department of Aerospace Engineering, University of Michigan, Ann Arbor, MI 48109, United States*

Abstract

The treatment of turbulent flows as finite-dimensional dynamical systems opens new paths for modeling and development of reduced-order descriptions of such systems. For certain types of dynamical systems, a property known as the inertial manifold (IM) exists, allowing for the dynamics to be represented in a sub-space smaller than the entire state-space. While the existence of an IM has not been shown for the three-dimensional Navier-Stokes equations, it has been investigated for variations of the two-dimensional version and for similar canonical systems such as the Kuramoto-Sivashinsky equation (KSE). Based on this concept, a computational analysis of the use of IMs for modeling turbulent flows is conducted. In particular, an approximate IM (AIM) is used where the flow is decomposed into resolved and unresolved dynamics, similar to conventional large eddy simulation (LES). Instead of the traditional approach to subfilter modeling, a dynamical systems approach is used to obtain the closure terms. In the *a priori* estimation of the AIM approach for the Kuramoto-Sivashinsky equation, it is shown that the small-scale dynamics are accurately reconstructed even when using only a small number of resolved modes. Further, it is demonstrated that the number of resolved variables needed for this reconstruction is dependent on the dimension of the attractor.

Keywords: Approximate inertial manifold, Kuramoto-Sivashinsky equation, Homogeneous isotropic turbulence, Reduced-order modeling

*Corresponding author
Email address: akramrym@umich.edu (Maryam Akram)

1. Introduction

Turbulent flows found in aerodynamics, propulsion, and other energy conversion systems pose an inherent computational challenge due to the broad range of temporal and spatial scales as well as the interaction of multiple physical processes [1]. Over the last few decades, a statistical approach to turbulence modeling has become the dominant framework, resulting in numerous practical tools including the Reynolds-Averaged Navier Stokes (RANS) and large eddy simulation (LES) approaches (although the latter is not often treated that way - rigorous mathematical basis is obtained only through a statistical notion [2, 3]). Such computational tools are extremely useful for extracting spatial statistical measures such as time-averaged velocity profiles, or higher-order moments such as RMS velocity. In general, much of the focus has been on statistically-stationary flows, where temporal averages may be used to estimate relevant statistical properties. However, within these applications mentioned above, there exists a range of problems for which assumptions regarding statistical stationarity are not strictly valid. This includes transient problems such as inlet unstart in scramjets [4, 5] or high-altitude reignition [6, 7], which deal with transition events driven partially by the chaoticity in the flow but are ultimately influenced by uncertainty in operating, boundary, or initial conditions. In these problems, a well-developed turbulent flow may not be present and such an assumption may lead to errors in predicting the probability of such transition events. Since tails of the distribution may drive transition events, there is a need to develop or explore techniques that do not explicitly rely on the statistical representation of unresolved quantities [8, 9].

In this context, dynamical systems-based methods are particularly useful. Starting from the mid-1980s, there has been growing recognition that treating an appropriately spatially-discretized set of governing equations as a finite-dimensional dynamical system provides access to properties about events that are otherwise difficult to assess using statistical tools. This approach to modeling complex systems has been particularly successful in weather prediction [10]. From a theoretical perspective, the focus has been on the structure of the dynamical system in phase space, which is composed of the N-dimensional state space defined by the degrees of freedom describing the discretized system. For instance, if a fluid domain is discretized using n_g grid points, and at each point n_v variables are solved, the state space dimension is $N = n_g \times n_v$. Note that this estimation is dependent on the type of numerical scheme used [11]. The spatial and temporal evolution of the turbulent flow can then be expressed as a trajectory in this state space. In many systems dominated by coherent structures, the long-term behavior of the system is dictated by dynamics confined to a low-dimensional subspace of the full N-dimensional state space. All trajectories of the system are attracted to this low-dimensional manifold, which contains the attractor of the system. Constantin et al. [12] showed that the dimension of the attractor scales nonlinearly with the Reynolds number of the flow. However, direct estimations of this attractor dimension for turbulent flows using the Kaplan-Yorke conjecture [13] showed that attractor dimensions are orders of magnitude lower than the number of degrees of freedom required by DNS [14, 15, 16].

In this regard, it is interesting to note that one of the original premises for the use of

dynamical systems is the development of reduced-order models, but this approach has been fraught with challenges for the following reasons [17]. First, the possible high-dimensionality of the attractor led to the conclusion that a highly reduced model cannot be easily determined [18]. Second, phenomenological approaches such as the intermittency model [19] did not directly provide a path to other spatially extended systems. Finally, there have been fundamental theoretical issues as to whether such reduced models can capture the chaoticity of the flow [17]. In light of these challenges, the recent focus on data-driven sciences has renewed interest in dynamical systems-based modeling of turbulent flows [20, 21, 22]. For instance, techniques for describing turbulent boundary layers have been formulated from these reduced-order modeling concepts [23].

In dissipative infinite-dimensional dynamical systems described by partial differential equations (PDEs), the long-time behavior of trajectories can be studied in an invariant finite-dimensional subset of phase space called the Inertial Manifold (IM) [24]. These manifolds, when they exist, attract all trajectories of the system exponentially and therefore contain the global attractor. The dynamics of the inertial manifold can be described by a finite-dimensional system of ordinary differential equations (ODE), called the inertial form, which completely describes the long-time dynamical behavior of the original infinite-dimensional system. In this vein, one approach considered in this work is the direct approximation of the inertial manifold [25, 26, 27, 28], where the dynamics of the system can be simplified in a subspace of the state space, naturally leading to the construction of a reduced-order model (ROM).

In the past, numerous studies have demonstrated the properties of inertial manifolds for specific systems [24, 29, 30]. These include analysis of the stability of the manifolds to perturbations [24], the exponential convergence of trajectories to the manifold [29], and questions regarding the suitability of this manifold approximation for representing the evolution of a dynamical system [29, 28]. These studies demonstrated that an IM is a reliable framework for describing the long-time dynamics of the system. Current proofs on the existence of the IM rely on the presence of arbitrarily large gaps in the spectrum of the linear operator of the dynamical system [24]. The existence of an inertial manifold has been proven for many dissipative PDEs [24, 31], describing different physical systems such as reaction-diffusion systems [32, 33, 34, 35], hydrodynamic instabilities [36, 37] and interfacial instabilities [32, 38, 24, 39]. However, it is important to recognize that these theoretical foundations are based on strong restrictions [24, 31], and a rigorous extension to real-life problems, such as an end application in multi-physics engineering processes, is a work in progress. Whether the spectral gap condition is necessary for the existence of the IM is still being explored, since other properties such as exponential tracking do not require this property. As such, it might be possible to prove the existence of the inertial manifold with weaker conditions [24].

Furthermore, these theoretical results cannot provide an explicit form for the inertial manifold. As a result, an approximation of the inertial manifold is necessary, which leads to the formulation of an approximate inertial manifold (AIM). AIMs can be developed to approximate either the true inertial manifold [40, 29, 33] or a neighborhood of the global attractor of the system [41, 42, 43, 27]. In this latter case, while the existence of an IM is

unknown, AIM still describes a subset of the phase space which approximates a neighborhood of the global attractor [28].

These studies demonstrated that the IM can be a powerful approach for developing reduced-order models that describe the underlying dynamical system. An example is the class of Galerkin-based IMs, also known as Galerkin manifolds [25, 28]. Here, the dynamics of the system are tracked on an AIM. The main assumption is that the dynamics in the complement space of the IM and full state-space are enslaved by the dynamics on the IM. In other words, the motion in the complement space responds instantaneously to changes in the trajectory on the AIM. While this assumption is justified by the theoretical studies discussed above [24, 29, 43], their validity needs to be scrutinized more rigorously. Many studies have been conducted on approximate inertial manifolds for dissipative systems, estimating their dimension and the rate of exponential convergence of dynamics to the AIM merely for dimension reduction [28, 44]. The concept of ROMs based on inertial manifolds for turbulence modeling was first introduced by Temam [43], where the interaction law between small and large scales guarantees the existence of an inertial manifold of the system. This work was followed by AIM-inspired ROM algorithms developed for different systems, including reaction-diffusion systems [24, 45], the Kuramoto-Sivashinsky equation [39, 29, 28] and the two-dimensional Navier-Stokes equations [43, 25, 46, 47]. In a more recent work, an AIM was developed as a suitable solution of the three-dimensional Navier-Stokes equations in Fourier space, and its properties were analyzed [48]. While almost all of these studies treat the governing equations using a Fourier-based spectral discretization, finite difference and finite volume-based PDE discretizations have also been considered [49, 50].

Recently, data-driven approximate inertial manifolds have been constructed using machine learning and data assimilation techniques [51, 52, 53, 54]. These techniques can be used to either determine the structure of the AIM model (including its dimension), or to track the dynamics with prior knowledge about its structure. Furthermore, AIMs enable the study of qualitatively different dynamical behaviors such as the transition to turbulence. For instance, bifurcations of the Kuramoto-Sivashinsky equation have been studied over a range of parameters using an AIM projected in two dimensions by symmetry reduction techniques [55]. Here, the manifold was computed and visualized for different dynamical behaviors of the system, which is intractable in the full state space.

Despite these extensive studies, there is limited computational exploration of AIMs and, in particular, their suitability for modeling turbulent flows. The focus of this work is to address this gap by systematically studying the AIM approach for a set of canonical systems. Here, an approximate inertial manifold is constructed for the one-dimensional Kuramoto-Sivashinsky equation and three-dimensional Navier-Stokes equations. The KSE has been studied extensively by approximate inertial manifolds; however, the range of parameters considered in previous works is such that the spatiotemporal chaotic behavior is not reached. Here, the KSE is studied in the fully chaotic regime to assess different aspects of AIM formulation. Also, the AIM approach is tested for homogeneous isotropic turbulence, which is the first such study to the authors' knowledge. As mentioned, an *a priori* study is conducted to examine the validity of AIM assumptions and to obtain an estimation of inertial manifold dimension. Accordingly, this study does not focus on model development,

since the full dimensional dynamical system is solved for the *a priori* estimation. However, the formulation provides a clear path to develop an AIM-based ROM as explained in Sec. 2. Results of both case studies are provided in Sec. 3. Finally, concluding remarks and future paths are discussed in Sec. 4.

2. Mathematical Formulation of AIM

Consider a set of partial differential equations that describe the evolution of any fluid system. The variables of interest are given by the set $\boldsymbol{\xi} = \{\xi_1, \xi_2, \cdots, \xi_{n_v}\}$, and the equations are written as

$$\frac{\partial \boldsymbol{\xi}}{\partial t} + \nabla \cdot \mathcal{N}(\boldsymbol{\xi}) + \nabla \cdot \mathcal{G}\boldsymbol{\xi} + S(\boldsymbol{\xi}) = 0, \tag{1}$$

where $\mathcal{N}$ is a nonlinear operator, $\mathcal{G}$ is a linear operator, and S is a volumetric source term. In the discussion below, this last term will be set to zero without loss of generality. In the context of non-reacting flows, $\boldsymbol{\xi}$ will include all transported variables such as momentum or energy. The nonlinear term $\mathcal{G}$ is typically the source of the multi-scale nature of this problem, producing a spectrum of length scales. Since the range of scales is dependent on some intrinsic parameter (such as Reynolds number), these equations are computationally intractable for any practical flow, and require some form of modeling that reduces the range of scales.

In this work, the modeling approach is based on a discretized form of Eq. 1 in an N-dimensional state space, where $\boldsymbol{v} \in \mathbb{R}^{n_g \times n_v}$ is the discrete vector of variables such that $\mathcal{D} : \boldsymbol{\xi} \rightarrow \boldsymbol{v}$, with $\mathcal{D}$ being the discretization operation. In this discretized form, the governing equations can be written as

$$\frac{d\boldsymbol{v}}{dt} + \mathcal{A}\boldsymbol{v} + \mathcal{F}(\boldsymbol{v}) = 0, \quad \boldsymbol{v}(t=0) = \boldsymbol{v}_0, \tag{2}$$

where $\boldsymbol{v}$ is the discrete set of variables, $\mathcal{A}$ is the discretized linear term, and $\mathcal{F}$ is the discretized nonlinear term. In order to apply the inertial manifold approach, $\mathcal{A}$ is taken to be a linear, self-adjoint operator defined on the Hilbert space $\mathcal{H}$. Let $\boldsymbol{S}(t) : v(0) \rightarrow v(t)$ be the semigroup of operators defining the solutions of Eq. 2. A subset $\mathcal{M} \subseteq \mathcal{H}$ is an inertial manifold if it satisfies the following properties [24]:

1. $\mathcal{M}$ is a finite dimensional Lipschitz manifold,
2. $\mathcal{M}$ is invariant, i.e., $\boldsymbol{S}(t)\mathcal{M} \subseteq \mathcal{M}$. for all $t \geq 0$,
3. $\mathcal{M}$ attracts exponentially all solutions of Eq. 2, i.e.,

$$\lim_{t \rightarrow \infty} \text{dist } (\boldsymbol{S}(t)\boldsymbol{v}_0, \mathcal{M}) = 0, \tag{3}$$

for every $\boldsymbol{v}_0 \in \mathcal{H}$.

In order to construct the reduced-order description, an orthogonal projection operator P is defined which splits the state-space into resolved ($\boldsymbol{u}$) and unresolved ($\boldsymbol{w}$) components:

$$\boldsymbol{u} = P\boldsymbol{v}, \quad \boldsymbol{w} = (I - P)\boldsymbol{v} = Q\boldsymbol{v}, \ \boldsymbol{v} = (\boldsymbol{u}, \boldsymbol{w}), \tag{4}$$

where $Q = I - P$, is the complement of the projection operation, and it maps its operand to the null-space of the projection operator P. Formally, IMs are realized as graphs of functions $\Phi : P\mathcal{H} \rightarrow Q\mathcal{H}$. For the form of the discretized system considered here (Eq. 2), the goal is to describe the dynamics in terms of $\boldsymbol{u}$ alone. Hence, the dimension of the projected space should be comparable to the dimension of the IM. Since $\mathcal{A}^{-1}$ is compact and self-adjoint, the set of eigenvectors of $\mathcal{A}$ form an orthonormal eigenbasis for the Hilbert space $\mathcal{H}$. Eigenvalues of $\mathcal{A}$ satisfy:

$$0 < \lambda_1 \leq \lambda_2 \leq \ldots, \lambda_j \rightarrow \infty \text{ as } j \rightarrow \infty \tag{5}$$

The main assumption of the inertial manifold theory is the existence of a relatively large gap in the spectrum of the linear operator, such that the dimension of the inertial manifold (m) can be determined by comparison between the largest eigenvalue (λ_m) of the linear operator projected onto the resolved subspace ($\mathcal{A}|_{P\mathcal{H}}$) and the smallest eigenvalue (λ_{m+1}) of the linear operator projected onto the unresolved subspace ($\mathcal{A}|_{Q\mathcal{H}}$) [24, 56]. Current theories on the existence of the inertial manifold strictly require a spectral gap, delineating time scales associated with the unresolved modes from those of the resolved modes; however, not all of the properties of the IM require the spectral gap condition to be satisfied. It might be possible to develop a theory of inertial manifolds which uses weaker conditions [24, 35].

Similar to prior formulations [24, 43], P is taken to be the projection onto the space formed by the first m eigenfunctions of the linear operator $\mathcal{A}$, spanning an $m \times n_v$-dimensional space, $\mathbb{R}^{m \times n_v}$. In this sense, resolved dynamics of the flow lie in this $m \times n_v$-dimensional space, where $m << n_g$. Such a decomposition of the state space into resolved and unresolved subspaces can be achieved by any set of orthogonal eigenbases of the full-dimensional state space. The dissipative linear operator, with a set of positive ascending eigenvalues, provides a clear path for decomposition into the resolved and unresolved subspaces. However, finding the eigenvalues of all of the linear and nonlinear terms of the governing equation can give more information about dominant dynamics. This method is more expensive computationally since the Jacobian of the dynamical system needs to be computed at each time step. Several reduced-order mechanisms are developed based on such decomposition, such as intrinsic low dimensional manifolds [57] and the computational singular perturbation [58, 59].

The goal is to describe the dynamical features of the flow in this lower-dimensional manifold instead of the full-dimensional system. Applying the projection operator to the discrete governing equations, the evolution equations for the resolved and unresolved fields can be obtained as

$$\frac{d\boldsymbol{u}}{dt} + \mathcal{A}\boldsymbol{u} + P\mathcal{F}(\boldsymbol{v}) = 0, \quad \boldsymbol{u}(t=0) = P\boldsymbol{v}_0, \tag{6}$$

and

$$\frac{d\boldsymbol{w}}{dt} + \mathcal{A}\boldsymbol{w} + Q\mathcal{F}(\boldsymbol{v}) = 0, \quad \boldsymbol{w}(t=0) = Q\boldsymbol{v}_0, \tag{7}$$

where $\boldsymbol{v}_0$ is the initial condition associated with the full state-space representation.

The main challenge in solving the resolved-scales equation is in the projected nonlinear term $P\mathcal{F}(\boldsymbol{v})$, which cannot be described using only $\boldsymbol{u}$. The goal is to estimate $\boldsymbol{w}$ given only

information of $\boldsymbol{u}$ and compute this nonlinear term. This is the typical closure challenge in turbulence modeling. The approach here is to leverage the unresolved-scales equation by utilizing the IM approximation: the dynamics of $\boldsymbol{u}$ directly determine the dynamics of $\boldsymbol{w}$. In other words, the components of $\boldsymbol{w}$ adjust to changes in $\boldsymbol{u}$ instantaneously. This modeling ansatz needs to be tested and will be discussed further in the example cases in the following sections. With the approximation $d\boldsymbol{w}/dt = 0$ [41]:

$$\mathcal{A}\boldsymbol{w} = -Q\mathcal{F}(\boldsymbol{v}), \tag{8}$$

which results in

$$\boldsymbol{w} = -\mathcal{A}^{-1}Q\mathcal{F}(\boldsymbol{u}, \boldsymbol{w}). \tag{9}$$

The above nonlinear equation can be iterated based on an arbitrary initial guess to obtain a converged solution for $\boldsymbol{w}$. The solution at iteration j is denoted by $\boldsymbol{w}^j$, with $\boldsymbol{w}^0 = 0$:

$$\boldsymbol{w}^j = -\mathcal{A}^{-1}Q\mathcal{F}(\boldsymbol{u}, \boldsymbol{w}^{j-1}). \tag{10}$$

In a majority of prior studies, only the first iteration is used [43, 46]. As a result, j is limited to 1 in this work, unless specified otherwise.

In this *a priori* study, the resolved modes $\boldsymbol{u}$ are obtained from direct computation of the full order system (direct numerical simulation or DNS), and the unresolved modes are approximated given the resolved modes. This does not directly provide a ROM, but an approach towards developing such a formulation is illuminated. With this in mind, the following section describes the application of this approach to two canonical flows, namely the Kuramoto-Sivashinsky equation (KSE) and homogeneous isotropic turbulence (HIT).

3. Application of AIM to canonical problems

3.1. Kuramoto-Sivashinsky equation-based spatiotemporal chaos

The KSE has been used as a surrogate for studying turbulence and interfacial instabilities [60, 61, 62]. Note that the existence of an IM has been proven for this system [39, 63]. The KSE is a convection-diffusion equation written as:

$$\begin{aligned} &\frac{\partial \xi}{\partial t} + \xi\frac{\partial \xi}{\partial x} + \frac{\partial^2 \xi}{\partial x^2} + \mu\frac{\partial^4 \xi}{\partial x^4} = 0 \ , \ x \in R, \ t > 0 \\ &\xi(x,t) = \xi(x+L,t); \ \xi(x,0) = g(x), \end{aligned} \tag{11}$$

where t is time, x is physical space, ξ is the solution of the equation, L is the spatial period, and μ is viscosity. The dynamics of the system are controlled by two parameters: L and μ. It is then possible to define a Reynolds number type parameter as $Re = \frac{L}{2\pi\sqrt{\mu}}$ [64], where the extent of spatiotemporal chaos is determined similar to the conventional use of this non-dimensional number. The range of scales in the system can be modified by changing Re. Here, viscosity is kept constant at $\mu = 0.001$, and the length of the domain is varied in the range of $[10\pi, 64\pi]$. The AIM will be investigated for this range of parameters.

In this work, spectral discretization is used, and the projection operator is defined in the spectral domain. Note that in this representation, the diffusion operator satisfies the properties needed for $\mathcal{A}$ (i.e., linear, unbounded, and self-adjoint). v is defined as the Fourier transform of ξ:

$$v(k,t) = \boldsymbol{F}(\xi(x,t)) = \frac{1}{L}\int_0^L \xi(x,t)e^{-iq_k x}dx, \tag{12}$$

where $q_k = \frac{2\pi k}{L}$, $k \in \mathbb{Z}$, and $\boldsymbol{F}$ is Fourier transform. In discretized form, n_F Fourier coefficients are used for v, denoted by v_k with $k \in [-n_F/2+1, n_F/2]$. The governing equation of the system in spectral space is obtained as a Galerkin projection of the Fourier modes:

$$\frac{d}{dt}v_k + (\mu q_k^4 - q_k^2)v_k + \frac{iq_k}{2}\sum_{\substack{1 \le |l| \le n_F/2 \\ 1 \le |k-l| \le n_F/2}} v_l v_{k-l} = 0. \tag{13}$$

Fourier modes with large wavenumbers have low amplitude and can be neglected at sufficiently large n_F. The discretized KSE, truncated at sufficiently large n_F, is solved using the exponential time difference fourth order Runge-Kutta method (ETDRK4) [65, 66] with standard 3/2 de-aliasing to generate DNS data. In the IM formulation, Eq. 13 can be arranged as Eq. 2 with the linear operator $\mathcal{A} = \mu q_k^4$ and $\mathcal{F}(v) = -q_k^2 v_k + i\frac{q_k}{2}\sum v_l v_{k-l}$ or their physical space analog. The KSE has two linear operators, but only one of them (μq_k^4) satisfies properties required by the theory of inertial manifolds. While the second-derivative term ($-q_k^2$) is responsible for instability at large scales, the fourth-derivative term provides damping at the small scales. In the spectral space, the resolved variables are $u = (v_{-m/2}, ..., v_{m/2})$, and the unresolved variables (w) are approximated with only one iteration by

$$w_k = -A^{-1}Q(\mathcal{F}(u))_k = \mu^{-1}q_k^{-4}\left(-\frac{i}{2}q_k \sum_{\substack{1 \le |l| \le m/2, \\ 1 \le |k-l| \le m/2}} (u)_l (u)_{k-l}\right). \tag{14}$$

The second-derivative term does not appear in Eq. 14 for $j = 1$ in Eq. 10. The initial condition of the dynamical system in physical space (Eq. 11) is $g(x) = \sin(x)(1+\cos(x))$. For the range of domain sizes considered here, this computation can become expensive. The required grid resolution is provided in Tab. 1. For this reason, an MPI-based domain decomposition approach is used to solve the system on distributed memory computers.

3.1.1. Numerical stability requirements

The KSE exhibits spatiotemporal chaos, where infinitesimal perturbations exponentially grow over time. Therefore, the numerical resolution (in time and space) used to resolve the system has a significant impact on the accuracy and stability of the solution. The range of scales found in the system increases with the length of the domain. As a result, the number of Fourier modes needed to resolve the dynamics also changes. Figure 1 shows a typical $x-t$ plot of the solution ξ for a Reynolds number 316.23 using 4096 Fourier modes. Initially, spatial variations retain the physical structure of the initial conditions. At

$t > 0.15$, transition to a chaotic regime is observed. However, with 1024 Fourier modes for the same Reynolds number, the solution becomes unstable after transition to the chaotic regime. These simulations with coarser resolution represent truncated systems without any subgrid model.

As expected, when sufficient spatial resolution is not available, the energy dissipation is not fully captured and there can be a pile-up of energy at the small-scales, which leads to numerical instability. Since one of the objectives of this work is to determine whether an AIM approximation is useful as a modeling path, the errors associated with the AIM process will be compared to those of the minimum resolution needed to evolve the governing equations stably. In other words, if the AIM approach shows good accuracy when using a smaller number of Fourier modes, it will provide a computational benefit when compared to the minimum resolution needed to solve the equations stably. Table 1 shows the required minimum resolution for the stability of the solution for different Re values as well as the maximum resolution used in the high fidelity solution of this study. This high fidelity simulation is called DNS in this study, since the governing equations are solved without any modeling. When discussing the AIM resolution (m in Sec. 2), the minimum resolution will be used as a reference.

Case	Length of domain	Re	N_{min}	N_{DNS}
A	10π	158.11	1024	2048
B	20π	316.23	2048	4096
C	36π	569.21	4096	8192
D	64π	1011.93	8192	16384

Table 1: Grid convergence study for different Re numbers. N_{min} denotes the minimum number of modes required to obtain a stable solution. N_{DNS} is the number of modes used to obtain the high fidelity solution.

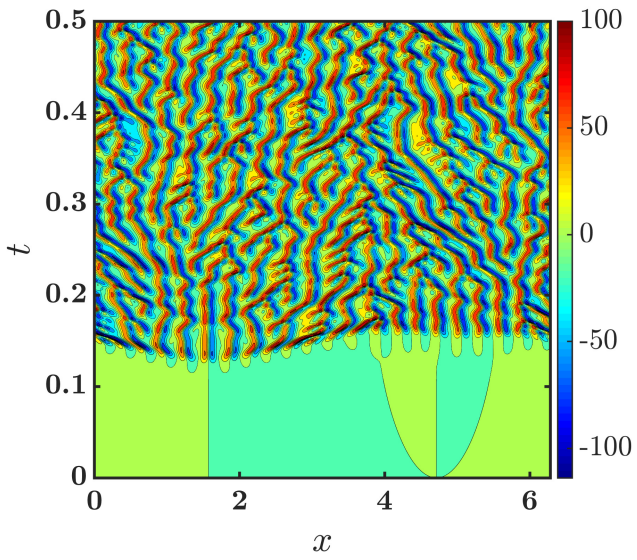

Figure 1: Solution of the KSE, $\xi(x,t)$, for $Re = 316.23$, $N_{DNS} = 4096$. Only part of the computational domain is shown.

3.1.2. Validity of AIM formulation

One of the key assumptions in the AIM method is that the linear operator dominates and controls the unresolved dynamics. In the KSE, the linear operator is dissipative in nature. If dissipation dominates the unresolved dynamics, the energy of high wavenumber modes is exponentially dissipative and asymptotically small. This fact reinforces the notion that long-time dynamics of the system lie in the inertial manifold. This assumption is evaluated using the energy budget for case A in Tab. 1. Figure 2 shows the energy budget for different quantities in the unresolved dynamics, each plotted using an AIM resolution of $m = 158$, which is equal to the number of linearly unstable modes in this case. The number of linearly unstable modes is found by linearizing Eq. 13 at its trivial solution and computing the eigenvalues of its linear operator. Eigenvalues with positive real part correspond to the linearly unstable modes. In this case, the eigenvalues are: $\lambda_k = q_k^2(1 - \mu q_k^2)$, which gives $[Re]$ eigenvalues with positive real part, where $[Re]$ is the integer part of Re.

To obtain the linear and nonlinear terms in Eqs. 6 and 7, the solution v from the high fidelity computation is projected onto the u and w spaces using the operators P and $Q = I - P$, respectively. For the KSE, P is the projector onto the span of the first m eigenvectors of the linear operator $A = \mu q_k^4$. The nonlinear operator ($\mathcal{F}$), discussed in Sec. 3.1 (Eq. 13), is computed using the DNS data and is then projected onto the resolved and unresolved spaces.

The energy budget, defined as the magnitude of each term for the evolution in spectral space, is shown in Figs. 2 and 3. For the unresolved scales, the magnitude of the linear term is comparable to that of the nonlinear term. This trend holds for the first unresolved mode as well as the average of all the unresolved modes. The linear operator gains more energy at the small scales because of the strong dissipative nature of the KSE. On the other hand,

for the resolved modes (shown in Fig. 3), the nonlinear term is substantial compared to the linear term, which is consistent with the chaotic nature of this system. It is also seen that the average of all resolved terms shows that both operators are of roughly similar magnitude. This is because the modes close to the cut-off wavenumber (i.e., close to $m = 158$) have a robust linear term (as seen for the first unresolved mode). As m is increased, the unresolved modes will be increasingly dominated by the linear operator.

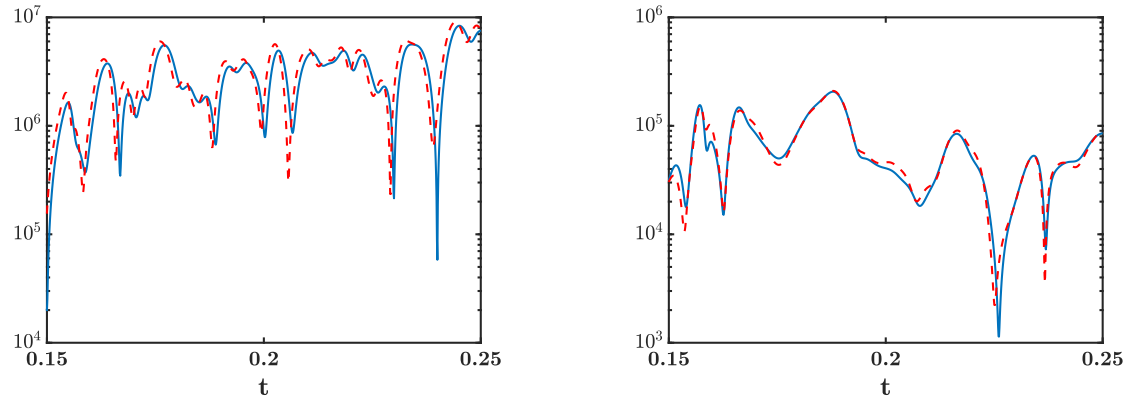

Figure 2: Energy budget for the unresolved dynamics (Eq. 7) of the KSE for $Re = 158.11$, $m = 158$. Linear operator ($\mathcal{A}w$): —, nonlinear operator ($Q\mathcal{F}(u, w)$): - -. Left: energy budget of the first unresolved mode, right: average energy budget of the unresolved dynamics.

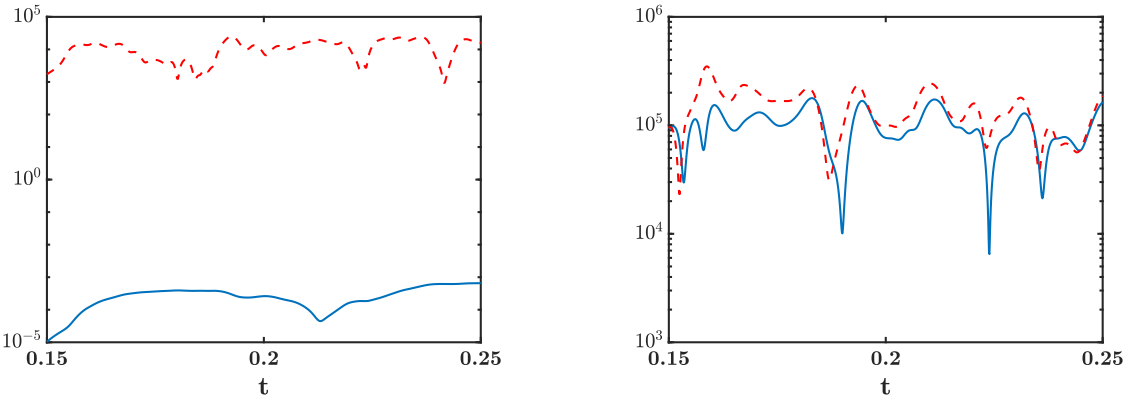

Figure 3: Energy budget for the resolved dynamics (Eq. 6) of the KSE for $Re = 158.11$, $m = 158$. Linear operator ($\mathcal{A}u$): —, nonlinear operator ($P\mathcal{F}(u, w)$): - -. Left: energy budget of the first resolved mode, right: average energy budget of the resolved dynamics.

3.1.3. Effect of resolution

The primary AIM outcome is the determination of the unresolved dynamics based on the evolution of the resolved scales. To understand the accuracy of this approach, an *a priori* analysis is conducted. As mentioned in Sec. 1, current theories can prove the existence of IM for some dissipative systems, although they cannot determine its dimension and topology

explicitly. Therefore, an estimation of the inertial manifold is essential. As the IM attracts all trajectories exponentially, its approximation must contain a thin neighborhood of the IM. Therefore, m should be larger than the dimension of the IM. However, obtaining this dimension is a computational challenge in itself, and is currently infeasible [67, 14, 11, 15]. Previous studies have estimated the dimension of IM for the KSE and provided an upper-bound scaling with different powers of Re [39, 28]. Here, the relation of the AIM accuracy to this dimension estimate is assessed.

For each Re, different resolutions of AIM are considered, and unresolved quantities are approximated by Eq. 14. They are then compared against the high fidelity solution of the dynamical system in spectral space. The results are first shown in Fig. 4, where the real part of the first unresolved mode is plotted. It is seen that as m increases, the AIM assumption becomes increasingly accurate, with the predicted field accurately tracking the exact quantity in time. Note that the number of resolved modes m is well below the minimum required to reach stability with a truncated system (Tab. 1).

Figure 5 shows the evolution of the average of unresolved quantities with time. It is seen that, similar to the first unresolved mode, increasing the approximation dimension (m) increases the accuracy of the results. However, the improvement is not as marked as for the first unresolved mode. From these figures, it is concluded that the modes closest to the resolved space are more responsive to the resolved-scale dynamics. This trend is shown more clearly in Sec. 3.1.4.

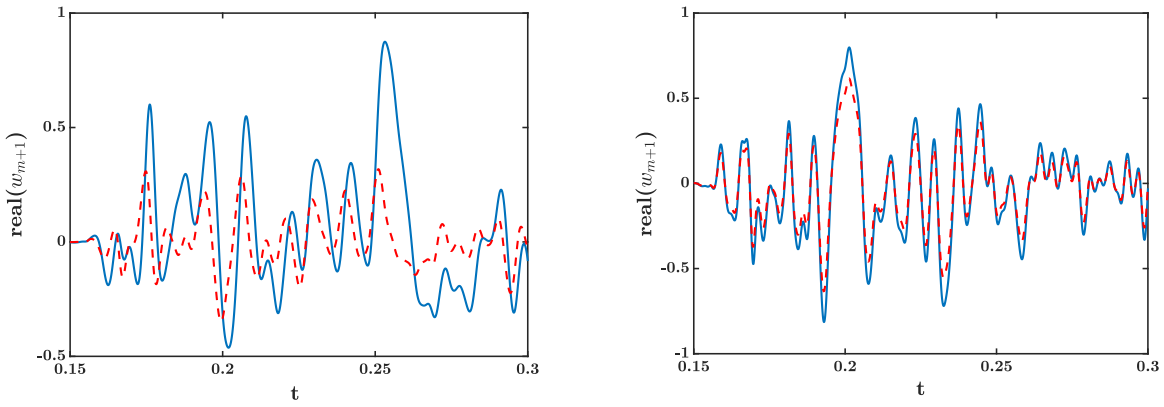

(a) $Re = 1011.93$, $m = 1024$ (b) $Re = 1011.93$, $m = 2048$

Figure 4: Effect of the AIM resolution on approximation of the dominant unresolved mode (w_{m+1}), DNS:—, AIM: - -.

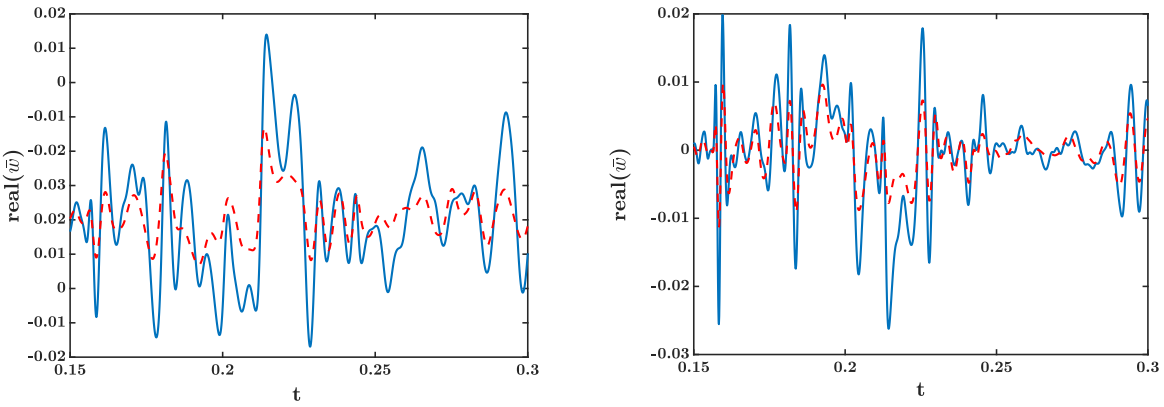

(a) $Re = 1011.93$, $m = 1024$ (b) $Re = 1011.93$, $m = 2048$

Figure 5: Effect of the AIM resolution on approximation of the average of unresolved dynamics ($\bar{w}$) , DNS:—, AIM: - -.

Even though the AIM estimation degrades at higher wavenumbers, the overall performance improves with increasing AIM resolution. Figure 6 shows the L_2-norm of the difference between the w field obtained using AIM (Eq. 14) and the unresolved sub-space of the full system solution (Eq. 13), expressed in the spectral space as a function of AIM resolution over the range of Re numbers. Regardless of the Re number used, after an initial reduction, the error appears to plateau before decreasing further. Incidentally, the switch from the plateau to the second convergence branch occurs when AIM resolution m exceeds the bifurcation parameter, Re. Given that prior work has shown that the dimension of the inertial manifold scales as Re [39, 28], this result suggests that strong convergence properties can be obtained for resolutions higher than the dimension of the inertial manifold. At low m, it is postulated that the initial error reduction occurs primarily because the resolved modes increasingly capture the key macroscopic features. A constant rate of convergence is not expected due to the highly nonlinear nature of the resolved scales dynamics [68].

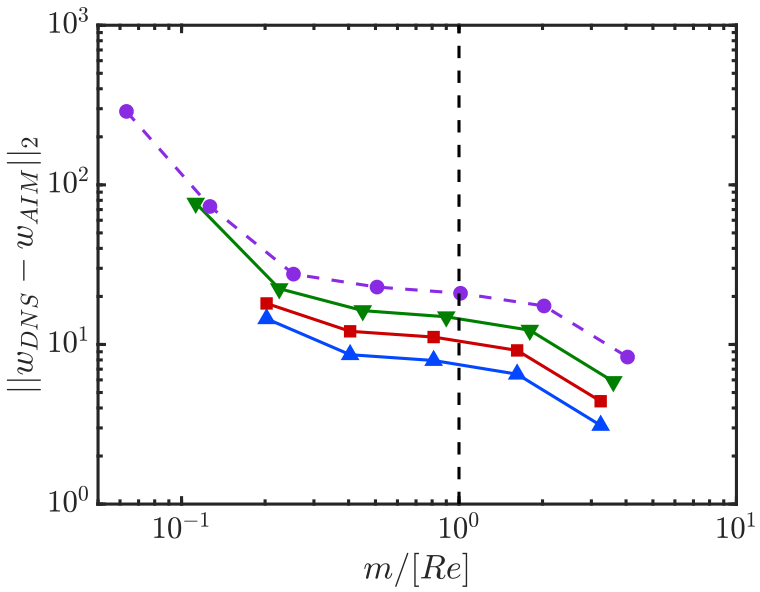

Figure 6: Effect of AIM resolution on estimation of unresolved dynamics $||w_{DNS} - w_{AIM}||_2$. $Re = 158.11$: ▲, $Re = 316.23$: ■, $Re = 569.21$: ▼, $Re = 1011.93$: ●. Vertical dashed line marks $m = [Re]$.

While the comparisons so far have been in spectral space, it is illustrative to consider the physical space features captured by the AIM model. For this purpose, two different resolutions of the AIM are considered for $Re = 158.11$. Figures 7 and 8 show the different fields for the AIM resolutions $m = 128$ and $m = 256$, corresponding to the full-dimensional reconstructed field and the unresolved dynamics, respectively. For a clearer representation of the small scales, only part of the simulation domain is shown for the chaotic regime ($t > 0.15$). Before the transition to this regime, the dynamics are laminar and captured by large wavelength resolved-scale modes.

Figure 7 compares the AIM-reconstructed fields ($\boldsymbol{F}^{-1}(u, w_{AIM})$) by two different AIM resolutions against the high fidelity (DNS) solution. The reconstructed field retains the features of the full field, even at the lower resolutions considered. For $m = 256$, the AIM-reconstructed field appears to retain most of the details of the flow qualitatively. However, these are full-dimensional fields reconstructed from the AIM approximation and resolved fields. In Fig. 8, comparison of the exact and approximated unresolved fields is revealing of the effect of AIM dimension in approximating the unresolved modes. In particular, it is seen that the extrema in the reconstructed field are smaller in magnitude in comparison to those of the original field. While this improves with the resolution, there remain differences in the spatiotemporal structures at $m = 256$.

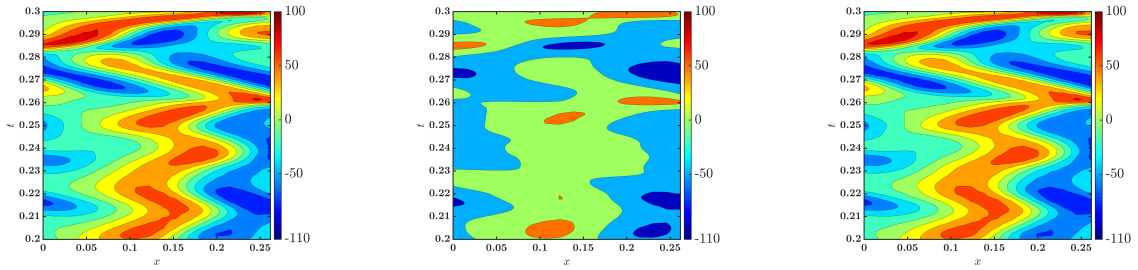

Figure 7: KSE solution in physical space for $Re = 158.11$, $n_g = 2048$. Left: full-dimensional solution ($\xi(x,t)$) obtained by DNS; middle: reconstructed solution by AIM ($\boldsymbol{F}^{-1}(u, w_{AIM})$) for $m = 128$; right: reconstructed solution by AIM ($\boldsymbol{F}^{-1}(u, w_{AIM})$) for $m = 256$.

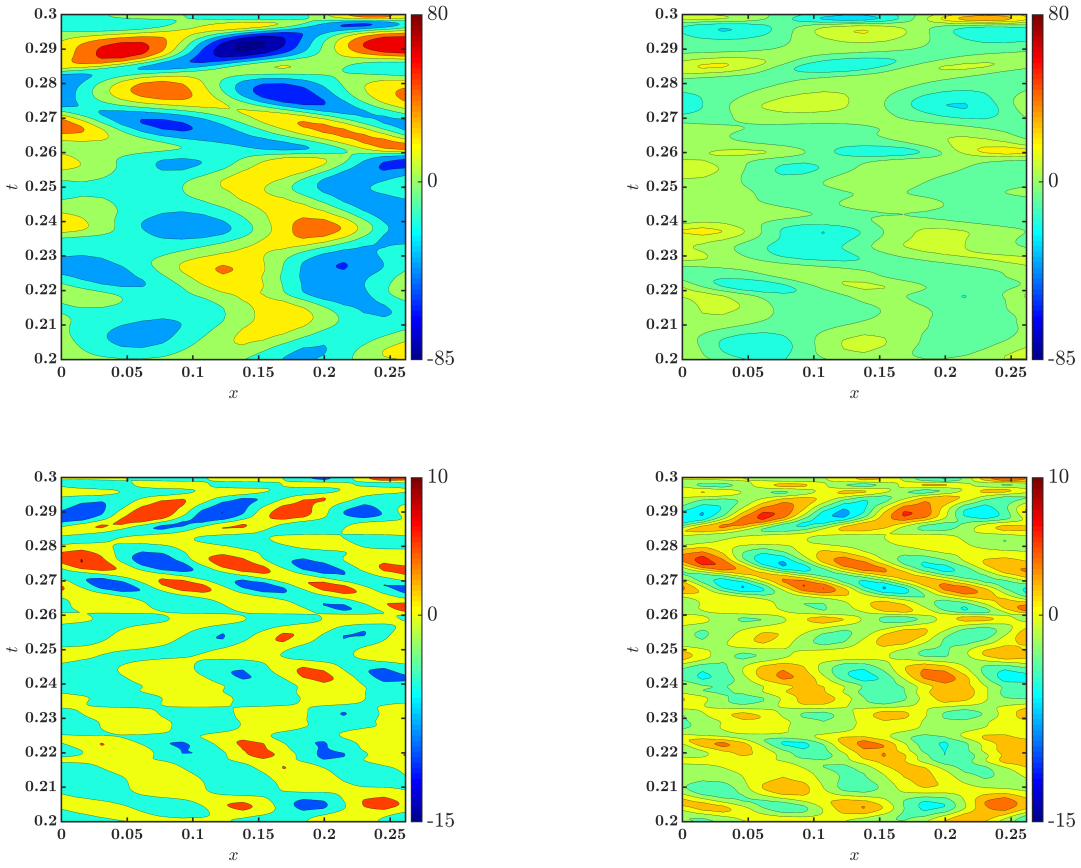

Figure 8: Unresolved dynamics of the KSE solution in physical space for $Re = 158.11$, $n_g = 2048$; Top left: DNS solution ($Q\xi(x,t)$) for $m = 128$, top right: AIM estimation by Eq. 14 for $m = 128$, bottom left: DNS solution ($Q\xi(x,t)$) for $m = 256$ and bottom right: AIM estimation by Eq. 14 for $m = 256$.

3.1.4. Accuracy of statistical features

While the focus so far has been on the ability of AIM to capture the dynamics of the underlying system, it is essential to understand the impact on the statistical properties of the

system. For this purpose, the two-point spatial correlation ($R(r,t) = \langle v(x,t)v(x+r,t)\rangle$) is computed for the DNS and AIM-reconstructed fields. Figure 9 (left) shows the convergence of AIM solution to the exact solution by increasing dimension of the AIM. Although the highest AIM resolution, (m), is significantly lower than the DNS resolution and the minimum resolution required for stability, it can capture the exact two-point correlation fairly accurately. Figure 10 shows the energy spectrum plotted in spectral space. Discrepancies in the modeled spectrum can be observed, especially at high wavenumbers. Nevertheless, AIM captures the energy of the largest unresolved scales quite accurately (for $|k| \in [50, 100]$), indicating that their dynamics are indeed enslaved to the largest resolved scales. However, the small-scales appear to have lower energy in the AIM reconstruction, indicating that the approach to the manifold is not purely determined by the scale-specific time-scale, which tends to be smaller at larger wavenumbers. This behavior is also seen in the spatial correlations of the unresolved dynamics alone, $\boldsymbol{w}$. Figure 9 (right) shows that for larger separations ($r/L > 0.05$) the two-point correlation is well represented by the AIM reconstruction of the small-scales, while the amplitude of these correlations is not captured at shorter separation distances.

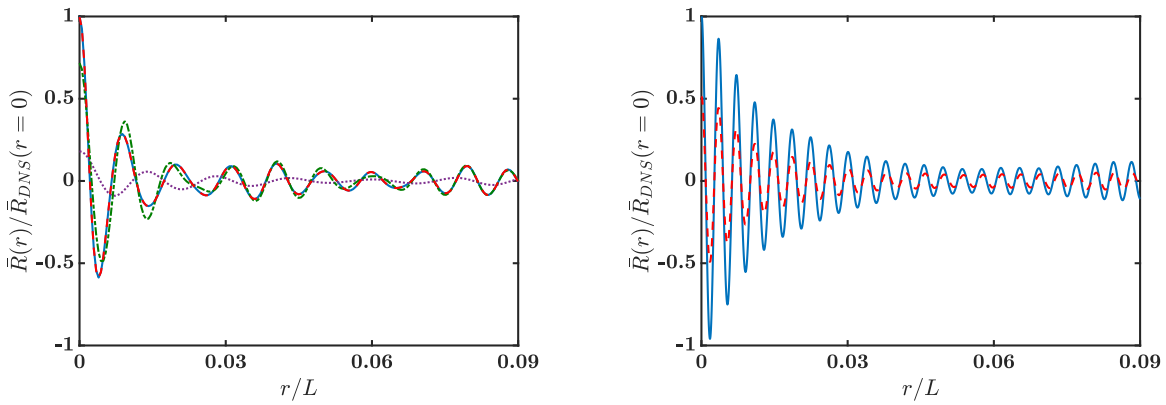

Figure 9: Spatial two-point correlation of velocity field in physical space for $Re = 158.11$. Left: convergence to DNS by increasing AIM resolution (m) obtained for full vector of variables (u, w); DNS: —; AIM, $m = 64$: • • •; AIM, $m = 128$: -·-; AIM, $m = 256$: - -. Right: Spatial-correlation of unresolved space (w) for $m = 256$. DNS: —; AIM: - -. In both plots, all values are normalized by the corresponding spatial correlation at $r = 0$ obtained by DNS.

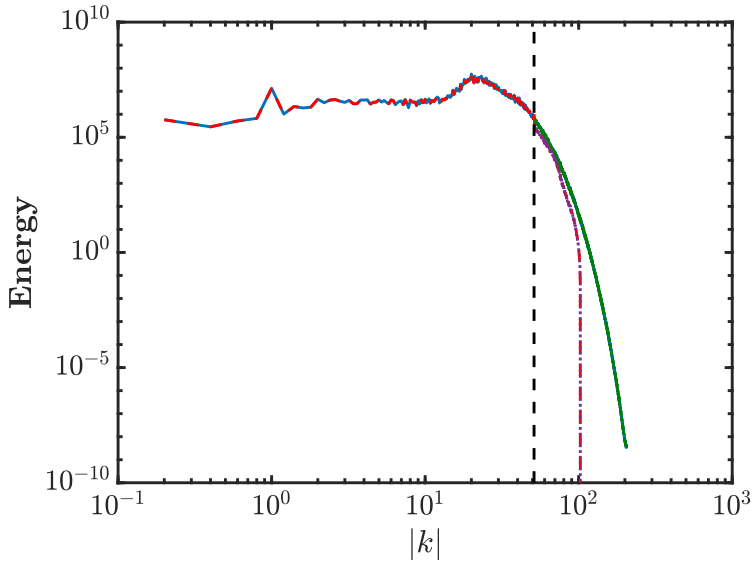

Figure 10: Energy spectrum for $Re = 158.11$, $m = 256$. DNS: —; AIM: - -; exact subgrid spectrum: -·-; subgrid spectrum approximated by AIM: . . . The vertical dashed line marks the cut-off wave number.

The energy spectrum and the two-point correlation show that the AIM approximation deteriorates at the smallest scales in the unresolved dynamics. However, the approximation can be improved by seeking the fixed-point solution of Eq. 10 with more iterations. Figure 11 (left) shows that with $j = 3$ in Eq. 10, the AIM approximation has improved considerably at higher wavenumbers, and the energy spectrum is reconstructed at the smallest scales. The rate of convergence is controlled by the quadratic nonlinearity in Eq. 10 which correlates different scales. Figure 11 (right) compares the normalized error of the energy spectrum of the unresolved modes obtained using different numbers of iterations. At each iteration, the number of unresolved modes correlated with the resolved dynamics is doubled because of the quadratic nonlinearity. By considering more iterations, the information in the resolved and larger unresolved scales is transferred to the smaller scales, which improves the performance of the approximation. Since the dimension of the unresolved dynamics is finite, increasing the number of iterations after some point does not improve the approximation anymore. In the discussions above, only the $j = 1$ solution is considered, since this provides a first order approximation of the unresolved dynamics.

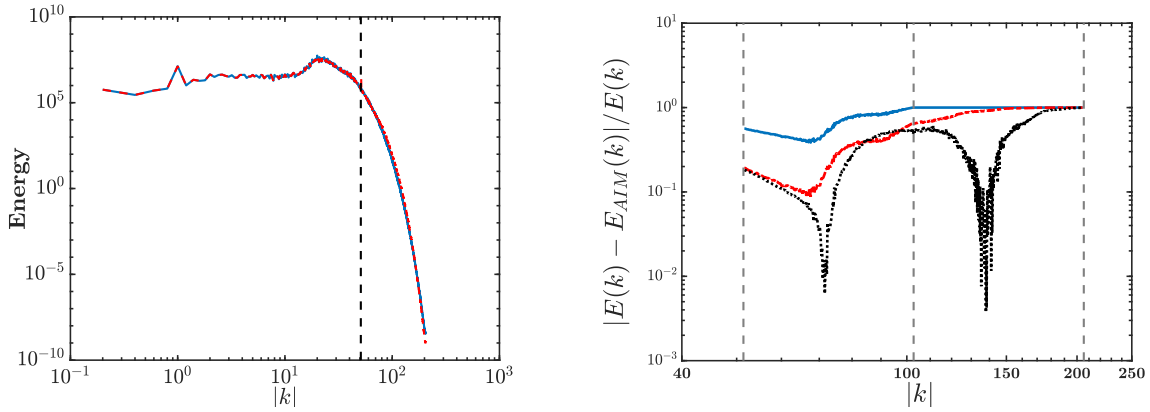

Figure 11: Left: Energy spectrum for $Re = 158.11$, $m = 256$. Unresolved dynamics are reconstructed by Eq. 10 with $j = 3$; DNS: —, AIM: - -. Right: Relative error in energy spectrum of the unresolved dynamics for $Re = 158.11$, $m = 256$, when unresolved dynamics are approximated by Eq. 10 with $j = 1$: —, $j = 2$: - - and $j = 3$: -·-. Vertical dashed lines mark wavenumbers k_m, $2k_m$ and $4k_m$.

3.2. Homogeneous isotropic turbulence

In this section, the performance of the AIM approximation is assessed *a priori* using a canonical turbulent flow configuration in a domain of $2\pi \times 2\pi \times 2\pi$ m. This problem represents a jump in complexity for two reasons: 1) the dimensionality of the discretized system is increased by orders of magnitude; 2) the existence of an IM has not yet been proven for the Navier-Stokes equations [24].

Here, the flow is considered incompressible, and the three-dimensional Navier-Stokes equations govern the state of the system:

$$\begin{aligned} &\frac{\partial \xi_i}{\partial t} + \xi_j \frac{\partial \xi_i}{\partial x_j} = -\frac{1}{\rho}\frac{\partial p}{\partial x_i} + \mu \frac{\partial}{\partial x_j}\left(\frac{\partial \xi_i}{\partial x_j}\right) + B\xi_i \\ &\frac{\partial \xi_i}{\partial x_i} = 0, \end{aligned} \tag{15}$$

where ξ_i is the velocity component in the i^{th} direction, p is the hydrodynamic pressure, μ is the kinematic viscosity and ρ is the density. Statistical stationarity is achieved by using a turbulent forcing technique that compensates for the viscous dissipation. A linear forcing scheme is used with a uniform constant coefficient B [69, 70]. Similar to the procedure used in the KSE, Eq. 15 is expressed in Fourier space as: $\xi_i = \sum_{\vec{k}} v_i(\vec{k}, t) e^{\vec{k}.\vec{x}}$. A Galerkin projection of the equation leads to a system of ODEs that govern the evolution of the Fourier coefficients $v_i(\vec{k}, t)$:

$$\begin{aligned} &\frac{d}{dt} v_i(\vec{k}, t) + \mu |k|^2 v_i(\vec{k}, t) - B v_i(\vec{k}, t) + k_i \frac{\vec{f}.\vec{k}}{|k|^2} - f_i = 0 \\ &f_i = -\boldsymbol{F}\left(\frac{\partial \xi_i \xi_j}{\partial x_j}\right)_{\vec{k}}, \end{aligned} \tag{16}$$

which is solved in a cube of side length 2π with periodic boundary conditions. Similar to the KSE, a pseudo-spectral method with dealiasing is used for the non-linear term. Exact time integration is used for the linear viscous term, and second-order Runge Kutta (RK2) is used for the other terms. Since small incompressibility errors can grow fast in a spectral formulation, it is necessary to remove the divergence error at every time step [71, 72]. At each time step, the velocity field is projected on the divergence-free space following the procedure explained in [71, App. A1]. Equation 16 can be rearranged as Eq. 2 using the linear operator $\mathcal{A} = \mu|k|^2$, with $\mathcal{F}(\boldsymbol{v})$ containing all other terms. It should be noted that the constant forcing term is not included in the linear operator since it does not satisfy properties required by the theory of inertial manifolds (Sec. 2). The projection operator that defines the resolved scales is parameterized using a three-dimensional wavenumber $k_{threshold}$ such that all the modes with wave numbers $\sqrt{k_x^2 + k_y^2 + k_z^2} \leq k_{threshold}$ are included in the resolved space. The number of modes satisfying this requirement is the dimension of AIM, (m). For example, $k_{threshold} = 2$ leads to $m = 23$. In the following sections, different values of $k_{threshold}$ are used to examine the convergence properties of AIM.

With the AIM approximation, the unresolved variables with wavenumber $\vec{k}$ can be approximated as:

$$\boldsymbol{w}_{\vec{k}} = -(\mu|k|^2)^{-1} Q\mathcal{F}(\boldsymbol{u}), \tag{17}$$

where $\boldsymbol{u}$ is the resolved velocity vector. As mentioned in Sec. 2, the unresolved dynamics can be approximated by solving Eq. 10 with a fixed-point iterative method. It can be shown that the AIM approximation satisfies continuity conservation. If the initial guess of the subgrid field is precisely divergence free, regardless of the iterative method, this approximation preserves this condition in the unresolved dynamics. However, if the initial guess of the unresolved velocity field does not satisfy the continuity equation, its residual error will grow exponentially. For the velocity vector corresponding to wavenumber $\vec{k}$ with initial guess $\boldsymbol{w}^0$ and j iterations in Eq. 10:

$$\begin{aligned} \bigtriangledown .\boldsymbol{w}_{\vec{k}}^0 &= \epsilon, \\ \bigtriangledown .\boldsymbol{w}_{\vec{k}}^j &= ((\mu|k|^2)^{-1} B)^j \epsilon, \end{aligned} \tag{18}$$

where ϵ is the residual of the continuity equation for the initial guess of the velocity vector. At each unresolved mode, the error grows at a rate proportional to the inverse of the wavenumber. Hence, the smallest unresolved scale (close to $|\vec{k}| = k_{threshold}$) has the highest growth rate.

3.2.1. HIT solution and numerical specifications

Four different spatial resolutions are used to investigate the accuracy of the AIM methodology for different Reynolds numbers. The simulation details are provided in Tab. 2. The Taylor microscale Reynolds number $Re_\lambda = \frac{u'\lambda_g}{\mu}$ and the Kolmogorov length scale $\eta = (\frac{\mu^3}{\epsilon})^{1/4}$ are monitored over the initialization time to make sure the turbulent field is fully developed, where λ_g is computed as $\sqrt{15\frac{\mu}{\epsilon}}u'$ [1, Chap. 6], u' is the fluctuating velocity and ϵ is the dissipation of turbulent kinetic energy. At each resolution, the flow statistics are monitored for approximately 1000 eddy turnover times (τ) to ensure a fully-developed, forced, statistically stationary flow field. The long transient time is chosen to make sure that the forcing method

does not lead to instability and energy pile-up at small scales. The AIM investigation period is started when the flow becomes statistically stationary. Figure 12 shows one snapshot of the magnitude of vorticity vector for different grid resolutions.

Case	Grid Resolution	Re_λ	$\eta/\Delta x$	Forcing coefficient (B)
I	32^3	15.7	1.22	0.1370
II	64^3	27.1	1.12	0.3275
III	128^3	39.34	1.18	0.825
IV	256^3	51.67	1.36	1.8

Table 2: Numerical setup for HIT.

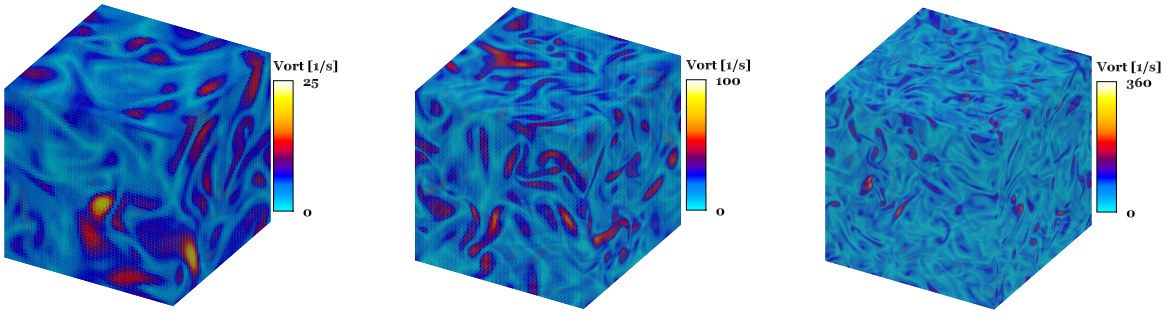

Figure 12: Instantaneous magnitude of vorticity vector obtained for different grid resolutions, left: $n_g = 64^3$, middle: $n_g = 128^3$ and right: $n_g = 256^3$.

3.2.2. Validity of AIM approximations

As discussed in Sec. 3.1.2 for the KSE, the key assumption in the AIM method is that the linear operator dominates the unresolved dynamics. In Navier-Stokes equations, the linear operator is the Stokes operator. Even though this operator is dissipative, and it possesses the required properties for AIM analysis (Sec. 2), it does not satisfy the spectral gap condition enforced by available theories on the existence of IM [24]. However, the existence of IM for Navier-Stokes equations might be proven by theories with more relaxed prerequisites. If the linear operator is dominant in the unresolved dynamics, these dynamics are asymptotically small, and the long-term dynamics of the system lie in the IM. In order to compare the prevailing effect of the linear term in the resolved and unresolved sub-spaces, the variation of the energy budget of the linear and nonlinear terms of the governing equations (Eqs. 6 and 7) are monitored over several eddy turnover times for case II in Tab. 2 with $k_{threshold} = 8$.

The linear and nonlinear terms, discussed in Sec. 3.2, are obtained from the DNS computation, where the full dimensional solution ($\boldsymbol{v}$) is projected onto the $\boldsymbol{u}$ and $\boldsymbol{w}$ spaces using the operators P and $Q = I - P$, respectively. The projection operator P is spanned by the first m eigenvectors of the linear operator $\mathcal{A} = \mu|\vec{k}|^2$, and the energy budget is defined as the magnitude of each term in spectral space. The same analysis for the KSE in Sec. 3.1.2

shows that in the resolved subspace, the nonlinear terms are considerably larger. While approaching the unresolved subspace, the linear term gains more energy. The linear and nonlinear terms are of the same order of magnitude in the unresolved subspace of the KSE. Figure 13 shows the variation of the energy budget for the unresolved (left) and resolved (right) dynamics. In the resolved subspace of the HIT, the nonlinear term is dominant. However, unlike in the KSE, the linear operator is not important in the unresolved dynamics. Even though the linear term becomes larger in the unresolved part, the nonlinear term remains important for all modes. This behavior is consistent over different AIM resolutions (different $k_{threshold}$ values) until the truncated system becomes as descriptive as the AIM.

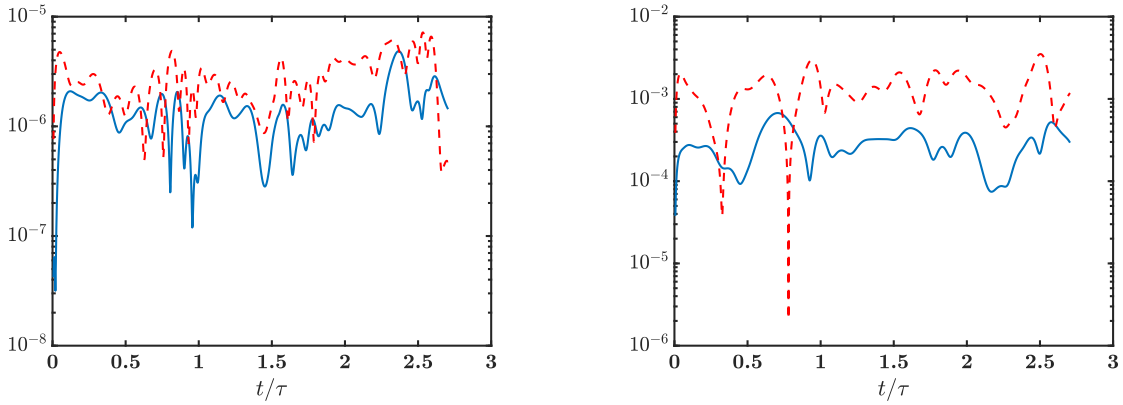

Figure 13: Energy budget of the governing equation for $n_g = 64^3$, $k_{threshold} = 8$, $m = 1153$, left: budget-study of the unresolved dynamics averaged over unresolved sub-space ($|\vec{k}| > 8$), linear term ($\mathcal{A}\boldsymbol{w}$): —, nonlinear term ($Q\mathcal{F}(\boldsymbol{u}, \boldsymbol{w})$): - -. Right: budget-study of the resolved dynamics for $k \leq k_{threshold}$ averaged over all resolved modes, linear term ($\mathcal{A}\boldsymbol{u}$): —, nonlinear term ($P\mathcal{F}(\boldsymbol{u}, \boldsymbol{w})$): - -.

3.2.3. Resolution of Approximate Inertial Manifold

For each case in Tab. 2, different values of $k_{threshold}$ are considered such that number of degrees of freedom for the largest approximate inertial manifold is around 30 percent of the degrees of freedom of DNS. The magnitude of the velocity field in physical space is shown in Fig. 14 for case IV (see Tab. 2) and $k_{threshold} = 32$. Figure 14 shows that the AIM-augmented field captures the dominant spatial features in the flow, even though the unresolved dynamics are overestimated.

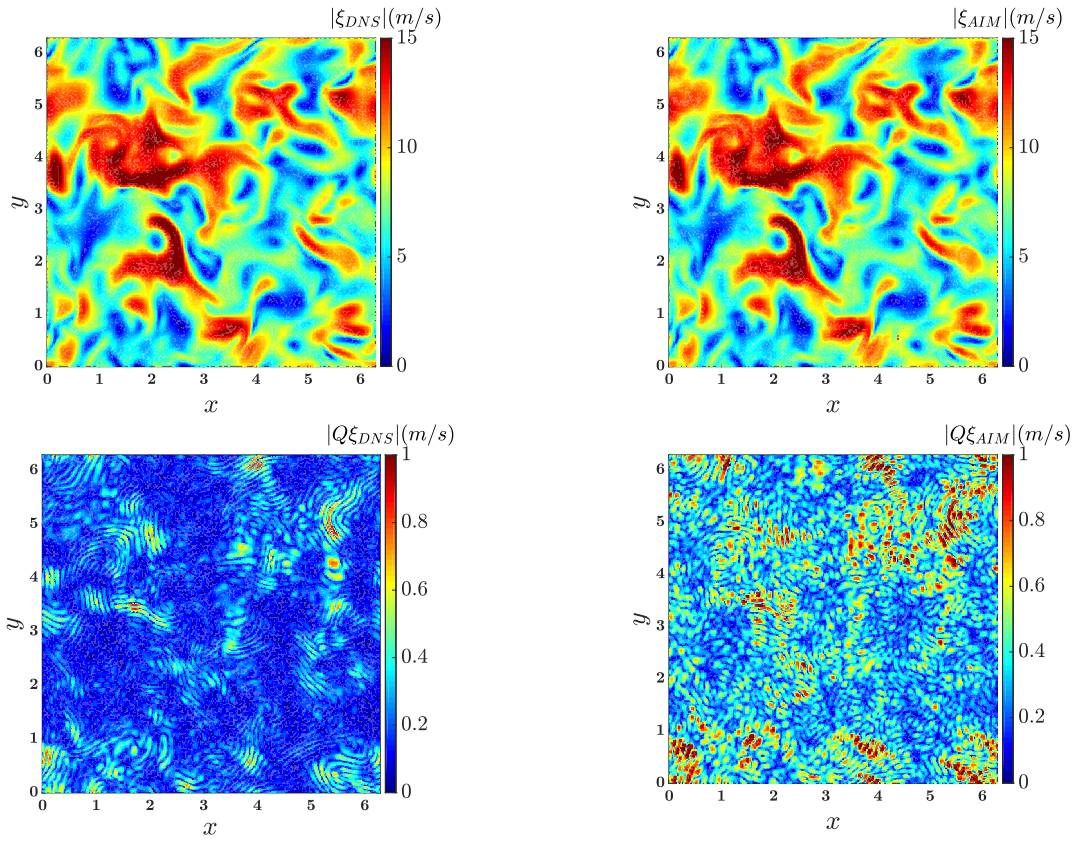

Figure 14: Magnitude of the velocity vector in a plane of the computational domain for $n_g = 256^3$, top left: DNS, top right: AIM reconstructed field, bottom left: DNS field projected onto the unresolved subspace, and bottom right: approximate unresolved dynamics by AIM. The last three fields are obtained for $k_{threshold} = 32, \quad m/n_g = 0.0042$.

Figures 15 and 16 show the effect of AIM resolution on accuracy. In all cases, increasing the number of resolved modes increases accuracy. Figure 16 shows that the dynamics of the sub-grid flow field are estimated with reasonable accuracy when using the information of the resolved modes alone (10 percent of the DNS modes). Figure 17 shows the L_2-norm of the difference between AIM estimation of the unresolved scales ($\boldsymbol{w}$) and the DNS solution as a function of AIM resolution (m). The error decreases with increasing resolution; similar to the results obtained with KSE, the rate of convergence is not constant. This behavior is consistent for all cases with different DNS resolutions.

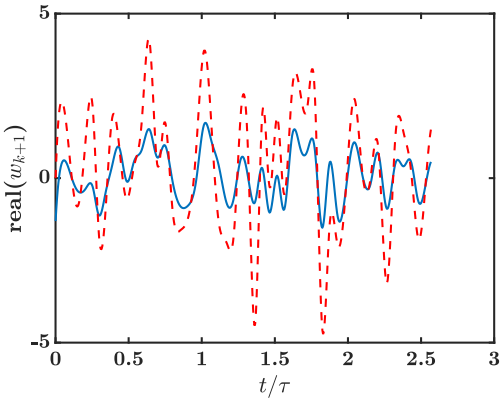

(a) $k_{threshold} = 32$, $m/n_g = 0.0042$

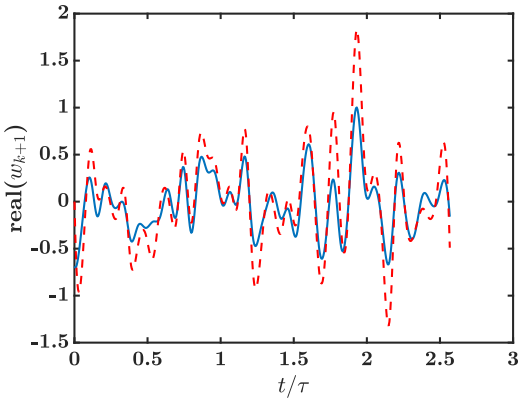

(b) $k_{threshold} = 72$, $m/n_g = 0.047$

Figure 15: Effect of AIM resolution (m) on the estimation of dominant unresolved mode for $n_g = 256^3$, left: $k_{threshold} = 32$, $m/n_g = 0.0042$, and right: $k_{threshold} = 72$, $m/n_g = 0.047$. DNS: —, AIM: - -.

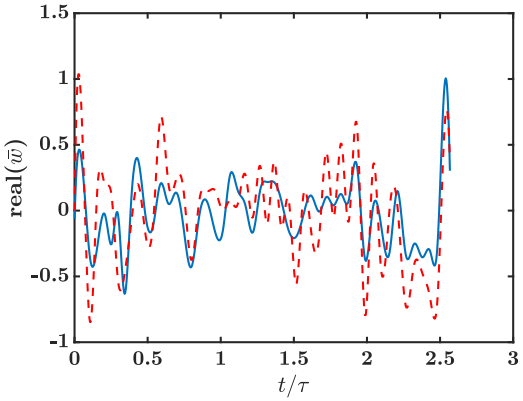

(a) $n_g = 256^3$, $m/n_g = 0.0042$

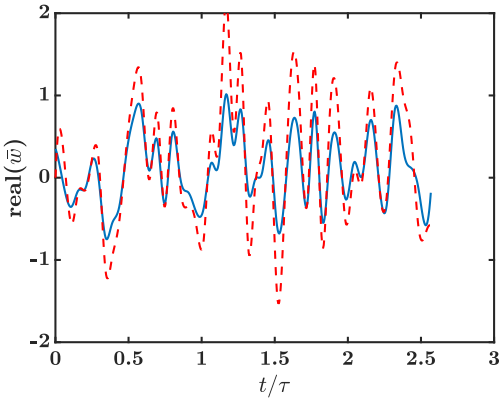

(b) $n_g = 256^3$, $m/n_g = 0.047$

Figure 16: Effect of AIM resolution (m) on the estimation of average unresolved dynamics. DNS: —, AIM: - -.

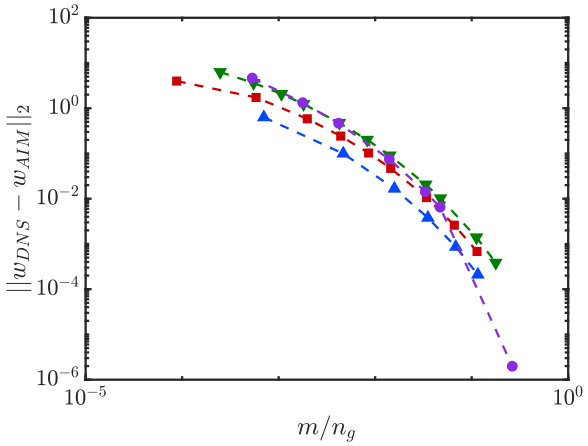

Figure 17: Effect of AIM resolution (m) on L_2-norm of the difference between exact and approximated unresolved dynamics $||\boldsymbol{w}_{DNS} - \boldsymbol{w}_{AIM}||_2$. $n_g = 32^3$: ▲, $n_g = 64^3$: ■, $n_g = 128^3$: ▼, $n_g = 256^3$: ●.

3.2.4. Statistical accuracy

Similar to the analysis of KSE in Sec. 3.1.4, the AIM modeling is assessed in terms of the statistics of the approximated flow field. The turbulent kinetic energy spectrum reconstructed with AIM is compared to that of DNS in Fig. 18 (top left), showing that the spectrum differs fundamentally from that of the KSE. The largest wavenumbers of the unresolved scales are not approximated accurately, which can cause stability issues in a modeling setup. This behavior can have two possible explanations which are discussed below.

In the governing equations of HIT, the forcing term is linear but counteracts dissipation, which is combined with other nonlinear terms in AIM formulation (Eq. 19).

$$\begin{aligned} &\frac{d}{dt}v_i(\vec{k},t) + \mu|k|^2 v_i(\vec{k},t) - Bv_i(\vec{k},t) + k_i\frac{\vec{f}.\vec{k}}{|k|^2} - f_i = 0 \\ &\mathcal{A}v_i = \mu|k|^2 v_i(\vec{k},t) \\ &\mathcal{F}(v)_i = -Bv_i(\vec{k},t) + k_i\frac{\vec{f}.\vec{k}}{|k|^2} - f_i \end{aligned} \tag{19}$$

Estimating the unresolved dynamics with only one iteration ($j = 1$) in Eq. 10 neglects the forcing term. The impact of this formulation is not critical at higher wavenumbers ($|\vec{k}| >> k_{threshold}$), where the dissipative linear operator ($\mathcal{A} \propto |\vec{k}|^2$) becomes more dominant compared to the constant linear forcing coefficient (B). Therefore, there is no energy overestimation at small scales. This may explain the discrepancy between AIM and DNS in the unresolved modes close to the cut-off wave number. To examine this explanation, the following experiment is conducted: the influence of the forcing term is removed by performing AIM on HIT and forcing only large scales to sustain turbulence. In this case, the forcing coefficient B is zero for unresolved modes. Figure 18 (top right) shows that AIM performance is improved when unresolved modes are not forced. However, there is still a small

overestimation of energy close to the cut-off wave number.

Furthermore, this persistent error in the energy spectrum may be related to the first order (one iteration, $j = 1$) approximation in Eq. 10. Approximating unresolved dynamics with additional iterations could be used to test this conjecture. For HIT, Eq. 10 can be written as

$$\boldsymbol{w}^{j}{}_{\vec{k}} = -(\mu|k|^2)^{-1} Q\mathcal{F}(\vec{\boldsymbol{u}}, \vec{\boldsymbol{w}}^{j-1}). \tag{20}$$

Considering Eq. 20 with $j = 1$, the nonlinear term only accounts for the interaction between the resolved scales. Implementing a fixed-point iterative method for solving Eq. 20 will include interactions among all scales in the resolved and unresolved sub-spaces. Previous studies of the two-dimensional Navier-Stokes equations have shown that the fixed-point iteration has a unique bounded solution with a convergence rate exponentially proportional to the smallest eigenvalue of the linear operator projected on to the unresolved subspace ($\mathcal{A}|_{Q\mathcal{H}}$) [27].

The unresolved dynamics are approximated by a preconditioned nonlinear Newton method. To ensure robustness, a successive over-relaxation (SOR) approach is used instead of the Newton scheme [73]. Figure 18 (bottom) shows that higher order estimation with only three iterations and SOR coefficient of 0.2 removes the energy build-up issue. This higher order estimation is more effective closer to the cut-off wave number, which is in the inertial range of the energy spectrum where the nonlinearity of energy cascade dominates the dynamics.

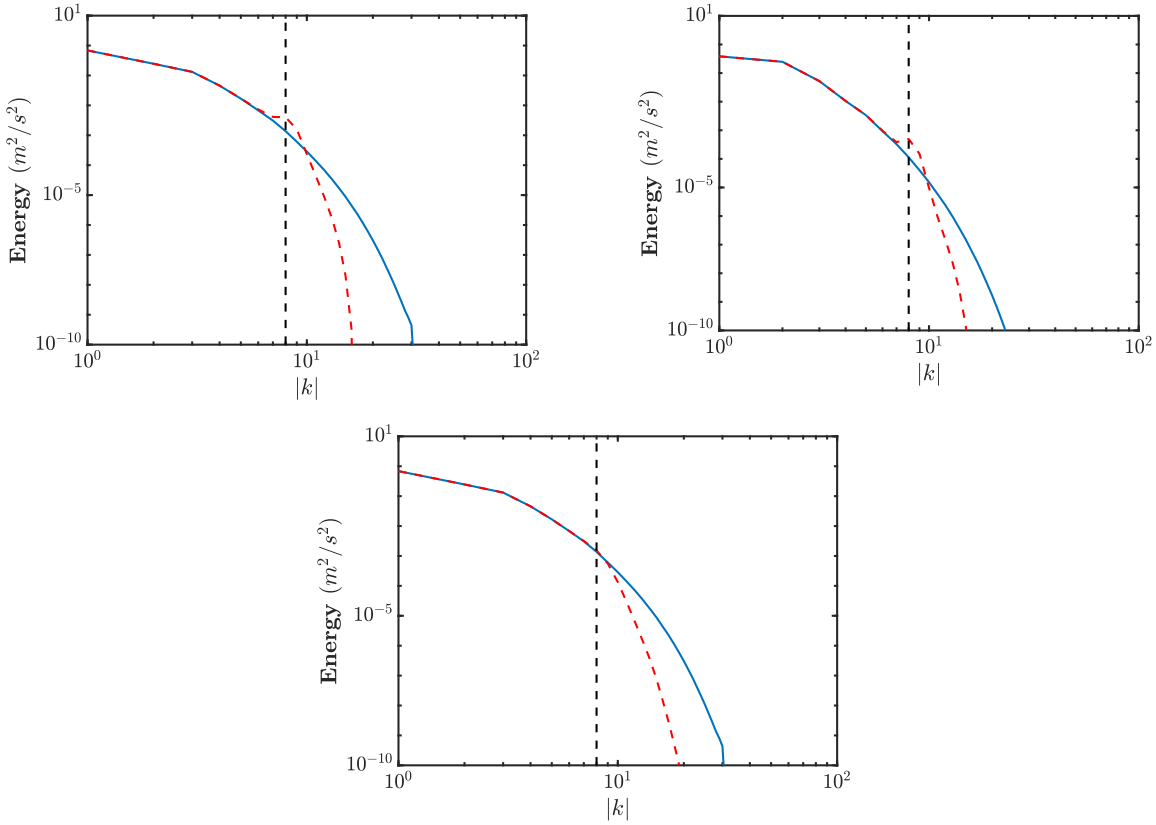

Figure 18: Energy spectrum reconstruction for $n_g = 64^3$, $k_m = 8$, $m = 1153$, top left: all scales are uniformly forced and $j = 1$ in Eq. 20, top right: only resolved scales are forced and $j = 1$ in Eq. 20, and bottom: all scales are uniformly forced with $j = 3$ in Eq. 20. Note that (m^2/s^2) denotes the energy units and is not related to the AIM dimension, m. DNS: —, AIM: - -.

3.2.5. Higher order statistics

In modeling the small-scale structures of the field from information at the large scales, the vorticity vector $(\vec{\omega})$, or its scalar equivalent, the enstrophy (z), is another important quantity describing the energy cascade between these scales. Given in Eq. 21, enstrophy measures dissipation of energy due to rotational or vortical motions, and its prediction leads to identifying vortex structures and measuring momentum dissipation from rotation.

$$\begin{aligned} \vec{\omega} &= \bigtriangledown \times \vec{\xi} \\ z &= \frac{1}{2}(\vec{\omega}.\vec{\omega}) \end{aligned} \tag{21}$$

Figure 19 compares the time evolution of the total energy and enstrophy, achieved with different AIM resolutions, with DNS. By increasing the number of resolved modes, the AIM approximation becomes more accurate. For $k_m = 32$, $m/n_g = 0.0042$, the difference between total energy estimated by AIM and computed from DNS is negligible, but there is a discernible error in total enstrophy prediction. This behavior shows that the dissipation

of energy is not captured accurately at the smallest scales.

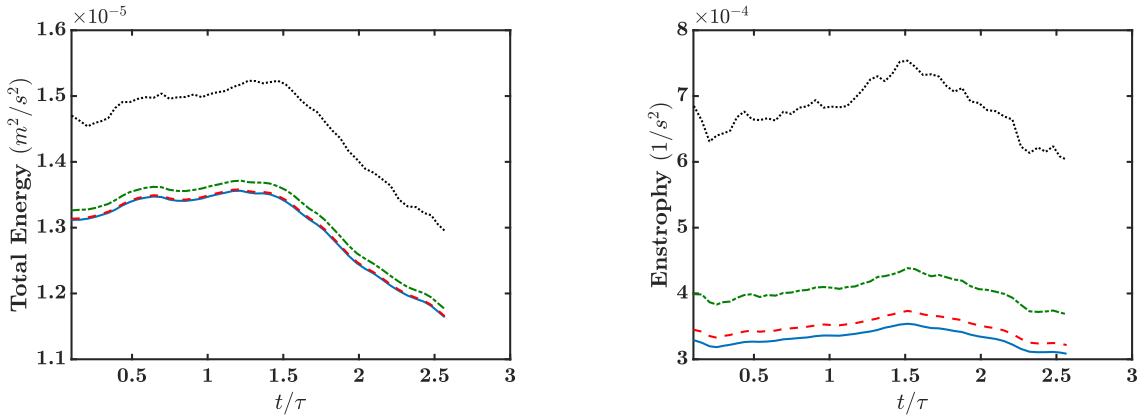

Figure 19: Effect of AIM-resolution on recovery of total energy and enstrophy for $n_g = 256^3$. The highest resolution of AIM contains only 0.4 percent of DNS modes. DNS: —, AIM with $k_m = 16$, $m/n_g = 5.33 \times 10^{-4}$: • • •, AIM with $k_m = 24$, $m/n_g = 0.0018$: -·-, AIM with $k_m = 32$, $m/n_g = 0.0042$: - -.

To further understand the method's ability to capture the spatial structure of the turbulent flow, the helicity field is also explored. Helicity is defined as the integral of the scalar product of the vorticity and velocity vectors, and is a measure of their alignment in the flow:

$$H = \int_V \vec{\xi} \cdot \vec{\omega} dV, \tag{22}$$

where the integral is over the computational domain. Helicity is related to nonlinear vortex stretching and impedes the cascade of energy between scales. While a higher helicity is associated with the coherent and long-lasting structures, a lower helicity indicates higher dissipation at small scales. Helicity density is defined as the dot product of the velocity and vorticity vectors: $\bar{h} = \langle \vec{\xi} \cdot \vec{\omega} \rangle$. Helicity is the integral of helicity density over the considered volume. Here, helicity density is computed at different AIM resolutions. Figure 20 shows that AIM with a sufficiently large dimension can capture helicity quite accurately. Helicity can also be studied as a dimensionless local quantity named relative helicity density [74],

$$h = \frac{\vec{\xi} \cdot \vec{\omega}}{|\vec{\xi}||\vec{\omega}|} = \cos(\theta), \tag{23}$$

which is defined as the cosine of the angle between velocity and vorticity vectors. In this definition, the instantaneous total velocity and vorticity fields are used. Regions with $h \approx \pm 1$ correspond to coherent large-scale structures. Previous studies suggest $\overline{h^2} = \overline{\cos^2\theta} \approx 0.333$ for a flat relative helicity density probability distribution function (PDF), where $\overline{h^2}$ is the average value of the PDF [74]. Larger or smaller values correspond to a greater or less helical behavior, respectively. Figure 20 (right) compares the fluctuating relative helicity density PDF approximated by AIM with DNS results. As shown, AIM modeling predicts more

dissipative vortical motion and fewer sustained structures, both in the PDF distribution and in the average helicity density of the field.

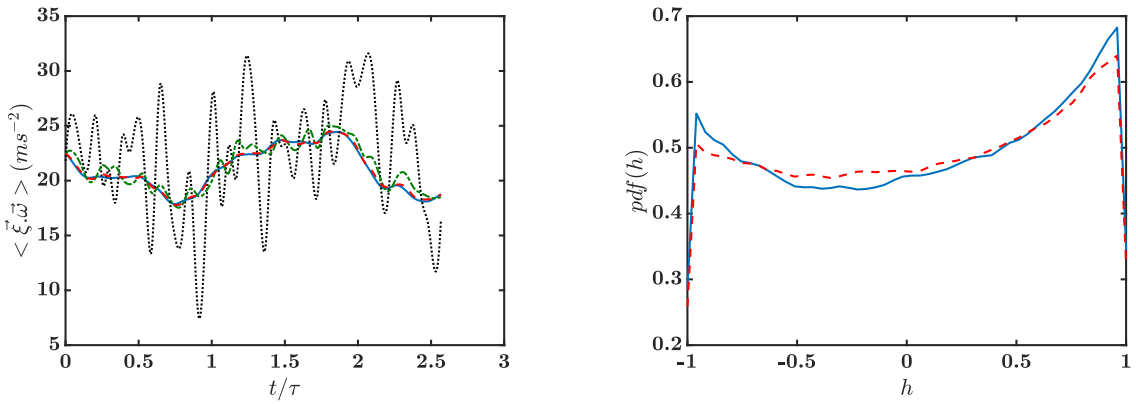

Figure 20: Prediction of helicity density by AIM. Left: convergence to DNS by increasing AIM resolution for $n_g = 256^3, 5.33 \times 10^{-4} < m/n_g < 0.0042$; DNS: —, AIM with $k_m = 16$: •••, AIM with $k_m = 24$: -·-, AIM with $k_m = 32$: - -. Note here that ms^{-2} denotes the helicity density units and is not related to the AIM dimension, m. Right: The relative helicity density PDF for $n_g = 128^3, k_{threshold} = 16$. ($\overline{h^2}_{DNS} = 0.3639$, $\overline{h^2}_{AIM} = 0.3540$); DNS: —, AIM: - -.

Higher-order moments of velocity derivatives provide information about the small-scale structure, including the transfer of energy between different scales and the inertial range. For this purpose, the derivative skewness is defined as:

$$S = -\frac{\langle (\frac{\partial \xi_1}{\partial x_1})^3 \rangle}{\langle (\frac{\partial \xi_1}{\partial x_1})^2 \rangle^{3/2}}, \tag{24}$$

with ξ_1 as the velocity component in x-direction, and $\langle \cdot \rangle$ denotes spatial average. By this definition, derivative skewness is positive, and it is related to vortex stretching and energy cascade in the dissipation range. Prediction of such higher-order statistics of small-scale quantities is essential for rare events consideration [1]. Figure 21 shows that AIM with sufficiently large dimension can track exact derivative skewness with significant dimension reduction ($m/N = 0.03$). Since the small scales are important for such derivative quantities, these results show that AIM can recover a portion of this information (Fig. 21, right).

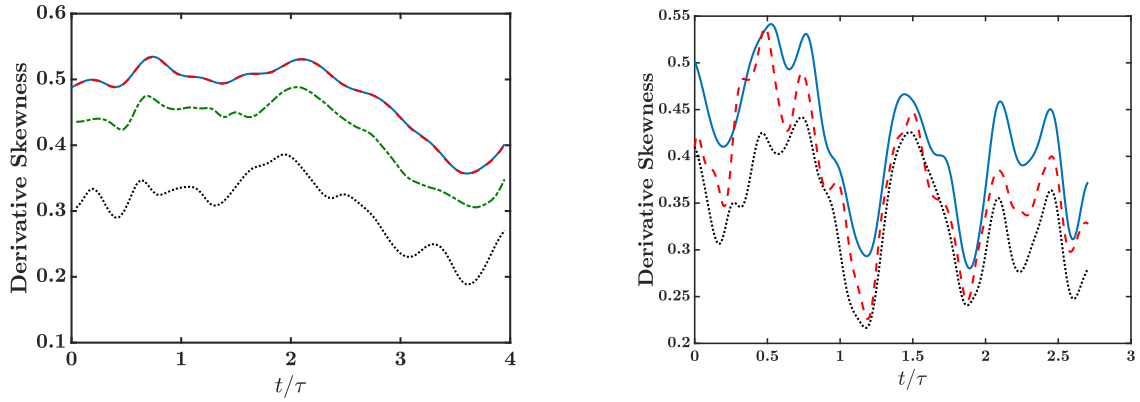

Figure 21: Prediction of velocity-derivative skewness by AIM. Left: convergence with resolution for $n_g = 128^3, 0.0018 < m/n_g < 0.0334$; DNS: —, AIM with $k_m = 12$: •••, AIM with $k_m = 16$: ·-·, AIM with $k_m = 32$: - -. Right: comparison of AIM with filtered DNS velocity field for $n_g = 64^3, k_m = 8, m/n_g = 0.0044$. DNS: —, AIM: - -, Projected DNS: ·-·.

4. Conclusions

In multiscale complex nonlinear systems, it is desired to predict the dynamical behavior without resolving all of the scales within the system through direct numerical simulations. In this context, the AIM methodology is a valuable alternative, naturally yielding a reduced-order approach while capturing the dominant dynamics of the problem. The focus of this study is to assess the suitability of the inertial manifold theory in the prediction of chaotic dynamical systems. Here, an *a priori* analysis of the AIM approximation to two canonical problems is studied: the one-dimensional KSE and HIT dictated by the three-dimensional Navier-Stokes equations.

The proposed AIM approximation is examined using a wide range of parameters in terms of the number of resolved scales (the dimension of the AIM) and the Reynolds or bifurcation numbers (directly proportional to the dimension of the approximate inertial manifold). In all configurations, for a sufficiently large dimension of the AIM, the dynamics of the unresolved variables are captured quite accurately. For the KSE, the statistics of the unresolved scales in the neighborhood of the inertial manifold are captured more accurately than the smaller scales farther away from the approximated IM. Smaller scales in the unresolved dynamics are less responsive to the dynamics of the IM, and there is a time-delay in their response. Similar behavior was observed for the HIT case. A higher order estimation of the unresolved dynamics, where the interactions between the resolved and unresolved dynamics are included, improves the AIM estimation of the unresolved dynamics.

The contribution of AIM to the unresolved dynamics can also be seen as a subgrid-scale model. By increasing the dimension of AIM, the approximated system was found to converge to the fully-resolved dynamics even in the HIT case, where the existence of an IM has not yet been analytically shown. The convergence rate was found to vary over the range of AIM dimension considered for each configuration of the system. This behavior was consistent for the range of Reynolds numbers considered. Interestingly, the convergence rates between

HIT and KSE are similar. Further studies at higher Reynolds number and more realistic flow configurations, such as wall-bounded flows, should be pursued.

Acknowledgements

This work is financially supported by AFOSR through grant FA9550-15-1-0378 with Dr. Chiping Li as program manager, and grant FA9550-16-1-0309 with Dr. Fariba Fahroo as program manager.

References

[1] S. B. Pope, Turbulent Flows, Cambridge University Press, 2000.
[2] J. A. Langford, R. D. Moser, Optimal LES formulations for isotropic turbulence, Journal of Fluid Mechanics 398 (1999) 321.
[3] R. J. Adrian, Conditional eddies in isotropic turbulence, The Physics of Fluids 22 (1979) 2065–2070.
[4] J. Wagner, K. Yuceil, N. Clemens, Velocimetry measurements of unstart of an inlet-isolator model in mach 5 flow, AIAA journal 48 (2010) 1875–1888.
[5] H. Koo, V. Raman, Large-eddy simulation of a supersonic inlet-isolator, AIAA journal 50 (2012) 1596–1613.
[6] B. Sforzo, J. Kim, J. Jagoda, J. Seitzman, Ignition probability in a stratified turbulent flow with a sunken fire igniter, Journal of Engineering for Gas Turbines and Power 137 (2015) 011502.
[7] Y. Tang, M. Hassanaly, V. Raman, B. Sforzo, J. Seitzman, A comprehensive modeling procedure for estimating statistical properties of forced ignition, Combustion and Flame 206 (2019) 158–176.
[8] M. Hassanaly, V. Raman, Computational tools for data-poor problems in turbulent combustion, in: AIAA Scitech 2019 Forum, 2019, p. 0998.
[9] V. Raman, M. Hassanaly, Emerging trends in numerical simulations of combustion systems, Proceedings of the Combustion Institute 37 (2019) 2073–2089.
[10] Kalnay, Atmospheric Modeling, Data Assimilation and Predictability, Cambridge University Press, 2003.
[11] M. Hassanaly, V. Raman, Numerical convergence of the Lyapunov spectrum computed using low Mach number solvers, Journal of Computational Physics 386 (2019) 467–485.
[12] P. Constantin, C. Foias, O. Manley, R. Temam, Determining modes and fractal dimension of turbulent flows, Journal of Fluid Mechanics 150 (1985) 427–440.
[13] J. L. Kaplan, J. A. Yorke, Chaotic behavior of multidimensional difference equations, in: Functional differential equations and approximation of fixed points, Springer, 1979, pp. 204–227.
[14] L. Keefe, P. Moin, J. Kim, The dimension of attractors underlying periodic turbulent Poiseuille flow, Journal of Fluid Mechanics 242 (1992) 1–29.
[15] M. Hassanaly, V. Raman, Ensemble-LES analysis of perturbation response of turbulent partially-premixed flames, Proceedings of the Combustion Institute 37 (2019) 2249–2257.
[16] M. Hassanaly, V. Raman, Lyapunov spectrum of forced homogeneous isotropic turbulent flows, Physical Review Fluids 4 (2019) 114608.
[17] G. Berkooz, An observation on probability density equations, or, when do simulations reproduce statistics?, Nonlinearity 7 (1994) 313.
[18] L. Biferale, Shell models of energy cascade in turbulence, Annual Review of Fluid Mechanics 35 (2003) 441–468.
[19] U. Frisch, P.-L. Sulem, M. Nelkin, A simple dynamical model of intermittent fully developed turbulence, Journal of Fluid Mechanics 87 (1978) 719–736.
[20] P. J. Schmid, Dynamic mode decomposition of numerical and experimental data, Journal of Fluid Mechanics 656 (2010) 5–28.

[21] C. W. Rowley, I. Mezić, S. Bagheri, P. Schlatter, D. S. Henningson, Spectral analysis of nonlinear flows, Journal of fluid mechanics 641 (2009) 115–127.
[22] S. L. Brunton, J. L. Proctor, J. N. Kutz, Discovering governing equations from data by sparse identification of nonlinear dynamical systems, Proceedings of the National Academy of Sciences (2016) 201517384.
[23] A. Sharma, B. McKeon, On coherent structure in wall turbulence, Journal of Fluid Mechanics 728 (2013) 196–238.
[24] C. Foias, G. R. Sell, R. Temam, Inertial manifolds for nonlinear evolutionary equations, Journal of Differential Equations 73 (1988) 309–353.
[25] R. Temam, Do inertial manifolds apply to turbulence?, Physica D: Nonlinear Phenomena 37 (1989) 146–152.
[26] S. Y. Shvartsman, I. G. Kevrekidis, Nonlinear model reduction for control of distributed systems: A computer-assisted study, AIChE Journal 44 (1998) 1579–1595.
[27] E. S. Titi, On approximate inertial manifolds to the Navier-Stokes equations, Journal of Mathematical Analysis and Applications 149 (1990) 540–557.
[28] M. Jolly, I. Kevrekidis, E. Titi, Approximate inertial manifolds for the Kuramoto-Sivashinsky equation: analysis and computations, Physica D: Nonlinear Phenomena 44 (1990) 38–60.
[29] C. Foias, G. R. Sell, E. S. Titi, Exponential tracking and approximation of inertial manifolds for dissipative nonlinear equations, Journal of Dynamics and Differential Equations 1 (1989) 199–244.
[30] F. Demengel, J.-M. Ghidaglia, Inertial manifolds for partial differential evolution equations under time-discretization: existence, convergence, and applications, Journal of Mathematical Analysis and Applications 155 (1991) 177–225.
[31] Y.-M. Chung, M. Jolly, A unified approach to compute foliations, inertial manifolds, and tracking solutions, Mathematics of Computation 84 (2015) 1729–1751.
[32] P. Constantin, C. Foias, B. Nicolaenko, R. Temam, Integral manifolds and inertial manifolds for dissipative partial differential equations, Math. Sci. Ser 70 (1988).
[33] M. Marion, Approximate inertial manifolds for reaction-diffusion equations in high space dimension, Journal of Dynamics and Differential Equations 1 (1989) 245–267.
[34] M. S. Jolly, Explicit construction of an inertial manifold for a reaction diffusion equation, Journal of Differential Equations 78 (1989) 220–261.
[35] J. Mallet-Paret, G. R. Sell, Inertial manifolds for reaction diffusion equations in higher space dimensions, Journal of the American Mathematical Society 1 (1988) 805–866.
[36] C. R. Doering, J. D. Gibbon, D. D. Holm, B. Nicolaenko, Low-dimensional behaviour in the complex ginzburg-landau equation, Nonlinearity 1 (1988) 279.
[37] J.-M. Ghidaglia, B. Héron, Dimension of the attractors associated to the Ginzburg-Landau partial differential equation, Physica D: Nonlinear Phenomena 28 (1987) 282–304.
[38] P. Constantin, C. Foias, B. Nicolaenko, R. Témam, Spectral barriers and inertial manifolds for dissipative partial differential equations, Journal of Dynamics and Differential Equations 1 (1989) 45–73.
[39] C. Foias, B. Nicolaenko, G. R. Sell, R. Temam, Inertial manifolds for the Kuramoto-Sivashinsky equation and an estimate of their lowest dimension (1988).
[40] E. Fabes, M. Luskin, G. R. Sell, Construction of inertial manifolds by elliptic regularization, Journal of Differential Equations 89 (1991) 355–387.
[41] C. Foias, O. Manley, R. Temam, Modelling of the interaction of small and large eddies in two dimensional turbulent flows, ESAIM: Mathematical Modelling and Numerical Analysis 22 (1988) 93–118.
[42] C. Foias, R. Temam, The algebraic approximation of attractors: The finite dimensional case, Physica D: Nonlinear Phenomena 32 (1988) 163–182.
[43] R. Temam, Induced trajectories and approximate inertial manifolds, ESAIM: Mathematical Modelling and Numerical Analysis 23 (1989) 541–561.
[44] W. Chen, Approximate inertial manifolds for 2D Navier-Stokes equations, Journal of Mathematical Analysis and Applications 165 (1992) 399–418.
[45] A. Adrover, G. Continillo, S. Crescitelli, M. Giona, L. Russo, Construction of approximate inertial man-

ifold by decimation of collocation equations of distributed parameter systems, Computers & Chemical Engineering 26 (2002) 113–123.
[46] F. Jauberteau, C. Rosier, R. Temam, A nonlinear Galerkin method for the Navier-Stokes equations, Computer Methods in Applied Mechanics and Engineering 80 (1990) 245–260.
[47] I. Chueshov, Approximate inertial manifolds of exponential order for semilinear parabolic equations subjected to additive white noise, Journal of Dynamics and Differential Equations 7 (1995) 549–566.
[48] J.-L. Guermond, S. Prudhomme, A fully discrete nonlinear Galerkin method for the 3D Navier-Stokes equations, Numerical Methods for Partial Differential Equations: An International Journal 24 (2008) 759–775.
[49] C. Foias, E. S. Titi, Determining nodes, finite difference schemes and inertial manifolds, Nonlinearity 4 (1991) 135.
[50] L. Margolin, D. Jones, An approximate inertial manifold for computing Burgers' equation, Physica D: Nonlinear Phenomena 60 (1992) 175–184.
[51] E. Bollt, Attractor modeling and empirical nonlinear model reduction of dissipative dynamical systems, International Journal of Bifurcation and Chaos 17 (2007) 1199–1219.
[52] A. J. Chorin, F. Lu, Discrete approach to stochastic parametrization and dimension reduction in nonlinear dynamics, Proceedings of the National Academy of Sciences 112 (2015) 9804–9809.
[53] F. Lu, K. K. Lin, A. J. Chorin, Data-based stochastic model reduction for the Kuramoto–Sivashinsky equation, Physica D: Nonlinear Phenomena 340 (2017) 46–57.
[54] W. Kang, J.-Z. Zhang, S. Ren, P.-F. Lei, Nonlinear Galerkin method for low-dimensional modeling of fluid dynamic system using POD modes, Communications in Nonlinear Science and Numerical Simulation 22 (2015) 943–952.
[55] N. B. Budanur, P. Cvitanović, Unstable manifolds of relative periodic orbits in the symmetry-reduced state space of the Kuramoto-Sivashinsky system, Journal of Statistical Physics 167 (2017) 636–655.
[56] N. Castañeda, R. Rosa, Optimal estimates for the uncoupling of differential equations, Journal of Dynamics and Differential Equations 8 (1996) 103–139.
[57] U. Maas, S. B. Pope, Simplifying chemical kinetics: intrinsic low-dimensional manifolds in composition space, Combustion and flame 88 (1992) 239–264.
[58] S. Lam, D. Goussis, Understanding complex chemical kinetics with computational singular perturbation, in: Symposium (International) on Combustion, volume 22, Elsevier, 1989, pp. 931–941.
[59] M. Valorani, S. Paolucci, The G-Scheme: A framework for multi-scale adaptive model reduction, Journal of Computational Physics 228 (2009) 4665–4701.
[60] D. Michelson, G. Sivashinsky, Nonlinear analysis of hydrodynamic instability in laminar flamesII. Numerical experiments, Acta Astronautica 4 (1977) 1207–1221.
[61] S. Lin, Finite amplitude side-band stability of a viscous film, Journal of Fluid Mechanics 63 (1974) 417–429.
[62] Y. Kuramoto, Diffusion-induced chaos in reaction systems, Progress of Theoretical Physics Supplement 64 (1978) 346–367.
[63] C. Foias, G. R. Sell, R. Temam, Variétés inertielles des équations différentielles dissipatives, Comptes rendus de l'Académie des sciences. Série 1, Mathématique 301 (1985) 139–141.
[64] J. M. Hyman, B. Nicolaenko, The Kuramoto-Sivashinsky equation: a bridge between PDE's and dynamical systems, Physica D: Nonlinear Phenomena 18 (1986) 113–126.
[65] A.-K. Kassam, L. N. Trefethen, Fourth-order time-stepping for stiff PDEs, SIAM Journal of Scientific Computing 26 (2005) 1214–1233.
[66] S. M. Cox, P. C. Matthews, Exponential time differencing for stiff systems, Journal of Computational Physics 176 (2002) 430–455.
[67] G. Benettin, L. Galgani, A. Giorgilli, J.-M. Strelcyn, Lyapunov characteristic exponents for smooth dynamical systems and for Hamiltonian systems; A method for computing all of them. Part 2: Numerical application, Meccanica 15 (1980) 21–30.
[68] S. B. Pope, Ten questions concerning the large-eddy simulation of turbulent flows, New journal of Physics 6 (2004) 35.

[69] C. Rosales, C. Meneveau, Linear forcing in numerical simulations of isotropic turbulence: Physical space implementations and convergence properties, Physics of Fluids 17 (2005) 095106.
[70] T. S. Lundgren, Linearly forced isotropic turbulence, in: CTR Annual Research Briefs, Center for Turbulence Research, CTR, Stanford University, 2003, pp. 461–473.
[71] M. Hassanaly, Extreme events in turbulent combustion, Ph.D. thesis, University of Michigan, Ann Arbor, MI, 2019.
[72] V. Eswaran, S. B. Pope, An examination of forcing in direct numerical simulations of turbulence, Computers & Fluids 16 (1988) 257–278.
[73] H. Woźniakowski, Numerical stability for solving nonlinear equations, Numerische Mathematik 27 (1976) 373–390.
[74] M. M. Rogers, P. Moin, Helicity fluctuations in incompressible turbulent flows, The Physics of Fluids 30 (1987) 2662–2671.